Fast simulation of 3D elastic response for wheel–rail contact loading using Proper Generalized Decomposition

Citation for the original published paper (version of record):

Ansin, C., Larsson, F., Larsson, R. (2023). Fast simulation of 3D elastic response for wheel–rail contact loading using Proper Generalized
Decomposition. Computer Methods in Applied Mechanics and Engineering, 417.
http://dx.doi.org/10.1016/j.cma.2023.116466

Computer Methods in Applied Mechanics and Engineering 417 (2023) 116466

Contents lists available at ScienceDirect

Comput. Methods Appl. Mech. Engrg.

journal homepage: www.elsevier.com/locate/cma

Fast simulation of 3D elastic response for wheel–rail contact loading using Proper Generalized Decomposition

Caroline Ansin [*], Fredrik Larsson, Ragnar Larsson

Division of Material and Computational Mechanics/ CHARMEC, Chalmers University of Technology, SE 412 96 Gothenburg, Sweden

ARTICLE INFO

Keywords:
Proper Generalized Decomposition
Model reduction
Elastic wheel–rail contact
Finite Element Method
Parametric loading
Separated representation

ABSTRACT

To increase computational efficiency, we adopt Proper Generalized Decomposition (PGD) to solve a reduced-order problem of the displacement field for a three-dimensional rail head exposed to different contact scenarios. The three-dimensional solid rail head is modeled as a two-dimensional cross-section, with the coordinate along the rail being treated as a parameter in the PGD approximation. A novel feature is that this allows us to solve the full three-dimensional model with a nearly two-dimensional computational effort. Additionally, we incorporate the distributed contact load predicted from dynamic vehicle–track simulations as extra coordinates in the PGD formulation, using a semi-Hertzian contact model. The problem is formulated in two ways; one general ansatz which considers the treatment of numerous parameters, some of which exhibit a linear influence, and a linear ansatz where multiple PGD solutions are solved for. In particular, situations where certain parameters become invariant are handled. We assess the accuracy and efficiency of the proposed strategy through a series of verification examples. It is shown that the PGD solution converges toward the FE solution with reduced computational cost. Furthermore, solving for the PGD approximation based on load parameterization in an offline stage allows expedient handling of the wheel–rail contact problem online.

1. Introduction

Rails in curved tracks are exposed to many contact scenarios resulting from large and varying vehicle loads, different curve radii as well as wheel and rail rim geometries. These scenarios can lead to rail damage, causing traffic interruptions, train delays, and expensive maintenance costs. Therefore, numerical computations are necessary to capture different contact scenarios to cost-effectively assess rail head damage. To evaluate degradation over time, it is essential to model various overrolling events that induce damage mechanisms such as wear, plastic deformation, and surface (or subsurface) initiated cracks due to rolling contact fatigue. However, performing these simulations can be computationally demanding, highlighting the need for methodologies that can reduce computational costs.

To calculate the long-term damage to the rail surface, there exists a framework [1–5] that considers multiple steps, applied in repetition (iteratively) between dynamic vehicle–track interaction for a given traffic situation, elastic–plastic wheel–rail contact, and accumulation of rail damage due to plasticity and surface wear to update the rail profile. In addition, surface rolling contact fatigue crack initiation is predicted. In this work, the simulation of the elastic–plastic contact is restricted to a meta-modeling strategy [1], and the subsequent analysis of the evolution of plastic deformation is reduced to a 2D analysis to allow efficient calculations. However, the assumptions pertinent to a two-dimensional analysis of the rail under contact are quite restrictive, and the contact load amplitude has to be scaled to obtain an "equivalent" load case.

---

[*] Corresponding author.
E-mail address: caroline.ansin@chalmers.se (C. Ansin).

https://doi.org/10.1016/j.cma.2023.116466
Received 7 July 2023; Received in revised form 22 August 2023; Accepted 18 September 2023

The present study aims to alleviate the restrictions related to two-dimensional analysis in the previous work [5] while maintaining a computationally efficient procedure. As a first step, the elastic response of a 3D rail head is investigated for different contact load scenarios. Thus, we account for the actual contact stress distribution and Poisson effects in the rail. Furthermore, contact stresses can act longitudinally along the rail. Even though the response is linear, traditional 3D Finite Element (FE) methods are computationally intensive and often impractical for considering very large amounts of loading scenarios, i.e., when the 3D solution needs to be solved many times.

To reduce computational complexity, some work has been done using the model reduction called Proper Generalized Decomposition (PGD). Unlike some other methods for reduced-order models, such as Proper Orthogonal Decomposition (POD) [6,7] and Reduced Basis (RB) [8], PGD is an a priori technique and does not require that the (approximate) solution to the complete problem is known [9]. Using PGD allows for efficient computations since the offline solution is computed only once, and the online solution can be determined efficiently. The offline solution is obtained using a successive enrichment strategy to give a numerical approximation of the unknown fields in a separate form for all solutions of the parameters within their respective intervals. The online phase is achieved efficiently because the inverse analysis only involves a postprocessing step of the precalculated parametric solution for a desired setup of the parameter values. This method originated from a space–time separation in the 1980s by Ladavèze et al. [10–13], but was further developed and generalized in the early 2000s by Chinesta et al. [9,14,15]. It can be applied to a variety of problems, including high-dimensional problems discussed in [14–17], parametric modeling [18–23] when there are many solutions to a problem, or when a quick solution is needed.

Bognet et al. and Giner et al. [21,24,25] proposed a domain decomposition to separate the displacement field $u(\boldsymbol{y}, x)$ for the in-plane $\boldsymbol{y} = (y, z)$ and out-of-plane x coordinates as

$$u(\boldsymbol{y}, x) \approx \sum_{n=1}^{N} \boldsymbol{Y}_n(\boldsymbol{y})\ X_n(x). \tag{1}$$

This separation allows for the representation of $u(\boldsymbol{y}, x)$ as a finite sum of unknown functions, also known as modes $\boldsymbol{Y}_n$ and X_n, respectively. This method reduces the 3D problem to a 2D computational complexity, as the computation of the 1D functions X_n is negligible compared to the computation of the 2D functions $\boldsymbol{Y}_n$. In this work, the same approach is used to solve the displacement field of a 3D solid rail head.

The PGD formulation allows for extra coordinates because the extra dimension does not impact the solvability of the problem. Examples of extra coordinates in parametric models may include material parameters as in [18–21] or boundary conditions considered in [9,22]. However, in this work, we would like to incorporate a distributed surface load to account for different contact conditions in the PGD framework. This type of load can be challenging to incorporate into the PGD framework since the optimality of the method depends on the separability of the solution. Cueto et al. and Zou et al. [20,23] previously addressed this challenge in the context of a moving unit load. However, in this case, we need to develop a similar approach but with a distributed surface load, since a contact area arises when two bodies in contact are pressed together.

There are many ways to model the wheel–rail contact, with the Hertzian theory of contact [26] being one of the most commonly used approaches. The Hertzian contact has an elliptical contact area described by a constant curvature and a parabolic pressure distribution. It is simple and fast but may not always apply to wheel–rail contacts that are locally conformal. Using the finite element method or CONTACT [27,28] provides higher accuracy, but comes with a higher computational cost. A semi-Hertzian approach called STRIPES [29,30] offers a compromise between accuracy similar to CONTACT, but with lower computational cost. In STRIPES, the contact area is estimated from the interpenetration area and is discretized in the lateral direction. Then a Hertzian-based formula is applied in the longitudinal direction to determine the stress distribution in each strip. Thus, this method allows for non-Hertzian conditions in the lateral direction, since the lateral curvature is not constant in the contact area. This is advantageous when the curvature of the contacting bodies varies or when the track is curved because flange contacts can occur at the wheel, which violates the conformal contact condition. The semi-Hertzian approach also facilitates a higher degree of separability of the solution in the context of PGD.

In this paper, we will employ the PGD formulation to compute the displacement field of a 3D elastic rail head subjected to different contact scenarios. The study consists of two parts, the first focusing on 3D modeling and the second on the parameterization of the distributed surface load. In the first part, a 2D model is used to represent the rail cross-section, while the rail coordinate serves as a parameter in the PGD approximation. To validate the results, we solve a 3D FE problem for a known Hertzian load. The second part deals with the parameterization of the distributed surface load, which is treated as extra coordinates to account for different contact scenarios. The STRIPES approach [29,30] is used to describe the surface load. The PGD approximation of the load is formulated in two ways where one is a general ansatz, whereas the second formulation is based on linearity. The proposed method allows for an efficient solution for different contact scenarios, since the PGD is solved only once for all specific parameter values within their respective intervals.

2. Problem description — 3D solid rail head analysis

The 3D solid rail head[1] Ω with the linear elastic material properties shown in Fig. 1 studied. An elliptical Hertz load [26] acts on the surface Γ_N but with restricted motion in the z-direction. The displacements at the bottom of the rail Γ_D are fixed. We are searching for the displacement field $\boldsymbol{u}(x, y, z)$ at any spatial coordinate $[x, y, z] \in \Omega$ in the rail head.

---

[1] The modeling choice to only consider the rail head is motivated by the local characteristic of the damage processes at the wheel–rail contact. Furthermore, it is possible to avoid geometric variation in the x direction that would otherwise occur if the entire cross section was considered such as the sleepers in the substructure

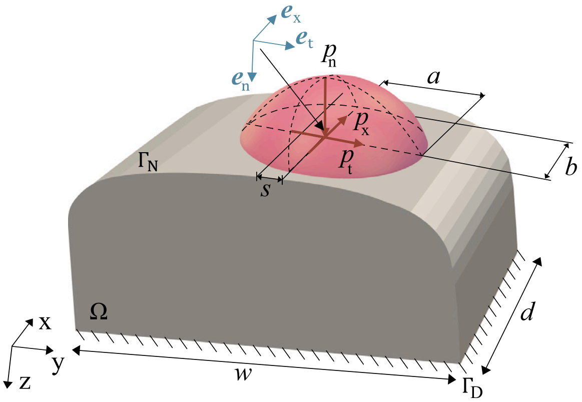

Fig. 1. Illustration of 3D rail section Ω with depth d and width w. The rail is subjected to a Hertz load [26] with semi-axes a and b. The load can move in the position s along the upper surface Γ_{N} but with a restricted motion in the x -direction. The maximum traction of the contact surface is p_{n}, p_{t}, and p_{x} in the corresponding directions $\boldsymbol{e}_{\mathrm{n}}$, $\boldsymbol{e}_{\mathrm{t}}$ and $\boldsymbol{e}_{\mathrm{x}}$. The basis vectors are defined locally from the rail profile at the center position of the contact area. The displacements are fixed at the bottom of the rail Γ_{D}.

We define the trial function space as $\mathbb{U} := \{\boldsymbol{v} \in [\mathbb{H}^1(\Omega)]^3 : \boldsymbol{v} = \boldsymbol{0} \text{ on } \Gamma_{\mathrm{d}}\}$, where $\mathbb{H}^1(\Omega)$ is the space of functions on Ω with square integrable derivatives of order zero and one. The weak form of the problem reads: find $\boldsymbol{u} \in \mathbb{U}$ such that

$$a(\boldsymbol{u}, \delta\boldsymbol{u}) = l(\delta\boldsymbol{u}) \quad \forall \delta\boldsymbol{u} \in \mathbb{U}, \tag{2}$$

where we define the bilinear and linear forms $a(\bullet,\bullet)$ and $l(\bullet)$, respectively, as

$$a(\boldsymbol{u}, \delta\boldsymbol{u}) = \int_{\Omega} \boldsymbol{\epsilon}[\delta\boldsymbol{u}] : \mathbf{E} : \boldsymbol{\epsilon}[\boldsymbol{u}] \;\, \mathrm{d}\Omega, \quad l(\delta\boldsymbol{u}) = \int_{\Gamma_{\mathrm{N}}} \boldsymbol{t} \cdot \delta\boldsymbol{u} \;\, \mathrm{d}\Gamma. \tag{3}$$

The strain tensor $\boldsymbol{\epsilon}$ is related to the displacement $\boldsymbol{u}$ as $\boldsymbol{\epsilon} = [\boldsymbol{u} \otimes \nabla]^{\mathrm{sym}}$ under the infinitesimal deformation assumptions. The stress tensor $\boldsymbol{\sigma}$ and the strain tensor $\boldsymbol{\epsilon}$ are related to the 4th order elasticity tensor $\mathbf{E}$ by Hooke's law $\boldsymbol{\sigma} = \mathbf{E} : \boldsymbol{\epsilon}[\boldsymbol{u}]$. A standard FE discretization can be applied to the weak form by introducing the FE-subspace $\mathbb{U}_{\mathrm{h}} \subset \mathbb{U}$.

The non-zero part of the traction $\boldsymbol{t}$ for an elliptic Hertz contact load [26] is expressed as

$$\boldsymbol{t}(\boldsymbol{y}, x) = \left(p_{\mathrm{n}}\boldsymbol{e}_{\mathrm{n}} + p_{\mathrm{t}}\boldsymbol{e}_{\mathrm{t}} + p_{\mathrm{x}}\boldsymbol{e}_{\mathrm{x}}\right)\sqrt{1 - \left(\frac{y-s}{a}\right)^2 - \left(\frac{x}{b}\right)^2}, \quad \left(\frac{y-s}{a}\right)^2 + \left(\frac{x}{b}\right)^2 < 1, \tag{4}$$

where s is the center position of the contact area on the rail, and p_{n}, p_{t}, and p_{x} are the maximum surface contact traction components corresponding to the normal ($\boldsymbol{e}_{\mathrm{n}}$), lateral ($\boldsymbol{e}_{\mathrm{t}}$) and longitudinal ($\boldsymbol{e}_{\mathrm{x}}$) directions at the rail surface, see Fig. 1. Also, a and b are the semi-axes of the elliptical contact patch in- and out-of-plane, respectively.

We approximate the shear stress to be proportional to the contact pressure, pertinent to the case of full slip conditions in Coulomb friction.[2] However, here we will let the amplitude of the shear stress components be governed by the amplitude of the applied load. Hence, the amplitudes p_n, p_t and p_x are independent variables.

Finally, we introduce the energy norm,

$$\|\boldsymbol{u}\|_a = \sqrt{a(\boldsymbol{u}, \boldsymbol{u})}, \tag{5}$$

which will be used for measurement of the solution, and its error, in subsequent sections.

3. 3D elastic PGD analysis of the rail for a known load

In this section, we outline the adopted PGD approach with the solution ansatz in terms of multiplicative separated in- and out-of-plane modes. In this development, a linear elasticity model is assumed for a known load, where the Hertzian load described in Section 2 is considered for the *fixed* surface load parameters p_n, p_t, p_x, a and b.

3.1. In- and out-of-plane separated PGD approximation

To speed up the computation of the weak form (2) of the 3D problem, we introduce a PGD approximation of the parametric solution with a plate decomposition, similar to what was done in [21,24,25]. The PGD approach is defined as a finite sum of separable

---

[2] Full slip in the Coulomb model would be characterized by the shear traction $\sqrt{(\boldsymbol{t})_{\mathrm{t}}^2 + (\boldsymbol{t})_{\mathrm{x}}^2} = \mu\ (\boldsymbol{t})_{\mathrm{n}}$, with μ being the coefficient of friction.

functions to approach a solution. It is assumed that the solution for the parameterized problem converges when approaching the approximation of the superposition of N modes

$$\boldsymbol{u}(\boldsymbol{y},x) \approx \boldsymbol{u}_N^{\mathrm{PGD}}(\boldsymbol{y},x) = \sum_{n=1}^{N} \boldsymbol{Y}_n(\boldsymbol{y})\; X_n(x), \tag{6}$$

where $\boldsymbol{y} = (y,z) \in \hat{\Omega}$ are the in-plane coordinates and $x \in I_{\mathrm{x}} = [-d/2, d/2]$ is the out-of-plane coordinate of the rail where the depth is defined as d. The modes $\boldsymbol{Y}_n(\boldsymbol{y})$ and $X_n(x)$ represent the unknown separated functions for the nth mode and depend on the parameters in- and out-of-plane, respectively. Thus, we have a $\boldsymbol{y}-x$ separated representation of the displacement field. The main influence of the track curvature comes from the tangential load component in the y-direction. Hence, we assume that the rail geometry is straight out-of-plane.

We can now decompose the geometry into $\Omega = (\hat{\Omega} \times I_{\mathrm{x}})$, $\Gamma_{\mathrm{N}} = (\hat{\Gamma}_{\mathrm{N}} \times I_{\mathrm{x}}) \cup \hat{\Omega} \times \{-d/2\} \cup \hat{\Omega} \times \{d/2\}$. Since $\boldsymbol{t} = \boldsymbol{0}$ at the end surfaces ($x = \pm d/2$), we can restate the forms in (2) and (3) as

$$a(\boldsymbol{v},\boldsymbol{w}) = \int_{I_{\mathrm{x}}} \int_{\hat{\Omega}} \boldsymbol{\epsilon}[\boldsymbol{w}] : \mathbf{E} : \boldsymbol{\epsilon}[\boldsymbol{v}]\; \mathrm{d}\hat{\Omega}\; \mathrm{d}x, \quad l(\boldsymbol{v}) = \int_{I_{\mathrm{x}}} \int_{\hat{\Gamma}_{\mathrm{N}}} \boldsymbol{t} \cdot \boldsymbol{v}\; \mathrm{d}\hat{\Gamma}\; \mathrm{d}x. \tag{7}$$

Furthermore, we consider $\Gamma_{\mathrm{D}} = \hat{\Gamma}_{\mathrm{D}} \times I_{\mathrm{x}}$. Hence, the homogeneous Dirichlet boundary condition can be expressed as $\boldsymbol{u} = \boldsymbol{0}$ on $\hat{\Gamma}_{\mathrm{D}}$, which is independent of x.

Assuming the first $N-1$ first terms have already been computed as

$$\boldsymbol{u}_{N-1}^{\mathrm{PGD}}(\boldsymbol{y},x) = \sum_{n=1}^{N-1} \boldsymbol{Y}_n(\boldsymbol{y})\; X_n(x), \tag{8}$$

we are seeking the modes $\boldsymbol{Y}_N(\boldsymbol{y}) \in \mathbb{Y}$ and $X_N(x) \in \mathbb{X}$ to obtain the further enriched PGD solution

$$\boldsymbol{u}_N^{\mathrm{PGD}}(\boldsymbol{y},x) = \boldsymbol{u}_{N-1}^{\mathrm{PGD}}(\boldsymbol{y},x) + \; \boldsymbol{Y}_N(\boldsymbol{y})\; X_N(x). \tag{9}$$

Hence, we seek updates in the spaces

$$\mathbb{Y} := \{\boldsymbol{v} \in [\mathbb{H}^1(\hat{\Omega})]^3, : \boldsymbol{v} = \boldsymbol{0} \text{ on } \hat{\Gamma}_{\mathrm{d}}\}, \quad \mathbb{X} := \mathbb{H}^1(I_{\mathrm{x}}), \tag{10}$$

whereby we note that the product $\boldsymbol{Y}_N X_N \in \mathbb{U}$.

In the spirit of Galerkin's method, the equations for determining modes $\boldsymbol{Y}_N$ and X_N are now established by testing (2) with $\delta\boldsymbol{u}(\boldsymbol{y},x) = \delta\boldsymbol{u}^{\mathrm{PGD}}(\boldsymbol{y},x) = \delta\boldsymbol{Y}(\boldsymbol{y})\; X_N(x) + \boldsymbol{Y}_N(\boldsymbol{y})\; \delta X(x)$ for $\delta\boldsymbol{Y}, \delta X \in \mathbb{Y} \times \mathbb{X}$.

Inserting the PGD approximation (9) into the weak form we obtain the problem of seeking $\boldsymbol{Y}_N, X_N \in \mathbb{Y} \times \mathbb{X}$ such that

$$a(\boldsymbol{Y}_N X_N, \delta\boldsymbol{Y} X_N) = l(\delta\boldsymbol{Y} X_N) - a(\boldsymbol{u}_{N-1}^{\mathrm{PGD}}, \delta\boldsymbol{Y} X_N) \quad \forall \delta\boldsymbol{Y} \in \mathbb{Y}, \tag{11a}$$

$$a(\boldsymbol{Y}_N X_N, \boldsymbol{Y}_N \delta X) = l(\boldsymbol{Y}_N \delta X) - a(\boldsymbol{u}_{N-1}^{\mathrm{PGD}}, \boldsymbol{Y}_N \delta X) \quad \forall \delta X \in \mathbb{X}. \tag{11b}$$

To solve (11) efficiently, we want to decompose the integration of the integrals as much as possible. We note that the strain appearing in (7) depends both on the in-plane and out-of-plane coordinates of the displacement, cf. [24]. It can be separated as

$$\boldsymbol{\epsilon}[\boldsymbol{u}^{\mathrm{PGD}}(\boldsymbol{y},x)] = \sum_{n=1}^{N} \hat{\boldsymbol{\epsilon}}[\boldsymbol{Y}_n(\boldsymbol{y})]\; X_n(x) + \boldsymbol{\epsilon}_{\mathrm{X}}[\boldsymbol{Y}_n(\boldsymbol{y})]\; \frac{dX_n(x)}{dx}, \tag{12}$$

where $\hat{\boldsymbol{\epsilon}}[\boldsymbol{Y}(\boldsymbol{y})] := [\boldsymbol{Y}(\boldsymbol{y}) \otimes \hat{\nabla}]^{\mathrm{sym}}$, $\boldsymbol{\epsilon}_{\mathrm{X}}[\boldsymbol{Y}(\boldsymbol{y})] := [\boldsymbol{Y}(\boldsymbol{y}) \otimes \boldsymbol{e}_{\mathrm{x}}]^{\mathrm{sym}}$ and $\hat{\nabla} = [\boldsymbol{I} - \boldsymbol{e}_{\mathrm{x}} \otimes \boldsymbol{e}_{\mathrm{x}}] \cdot \nabla$ is the in-plane gradient and $\boldsymbol{e}_{\mathrm{x}}$ is the out-of-plane basis vector, see Fig. 1. When the arguments of the bilinear form $a(\bullet,\bullet)$ are products of modes, it can be written as

$$a(\boldsymbol{Y}X, \boldsymbol{Y}^*X^*) = \sum_{I=1}^{4} m_I(X,X^*)\; a_I(\boldsymbol{Y},\boldsymbol{Y}^*), \tag{13}$$

with the bilinear forms on the separated domains, m_I, and a_I are defined according to

$$m_1(X,X^*) = \int_{I_{\mathrm{x}}} X\; X^*\; \mathrm{d}x, \qquad a_1(\boldsymbol{Y},\boldsymbol{Y}^*) = \int_{\hat{\Omega}} \hat{\boldsymbol{\epsilon}}[\boldsymbol{Y}] : \mathbf{E} : \hat{\boldsymbol{\epsilon}}[\boldsymbol{Y}^*]\; \mathrm{d}\hat{\Omega}, \tag{14a}$$

$$m_2(X,X^*) = \int_{I_{\mathrm{x}}} \frac{dX}{dX}\; X^*\; \mathrm{d}x, \qquad a_2(\boldsymbol{Y},\boldsymbol{Y}^*) = \int_{\hat{\Omega}} \hat{\boldsymbol{\epsilon}}[\boldsymbol{Y}] : \mathbf{E} : \boldsymbol{\epsilon}_{\mathrm{X}}[\boldsymbol{Y}^*]\; \mathrm{d}\hat{\Omega}, \tag{14b}$$

$$m_3(X,X^*) = \int_{I_{\mathrm{x}}} X\; \frac{dX^*}{dx}\; \mathrm{d}x, \qquad a_3(\boldsymbol{Y},\boldsymbol{Y}^*) = \int_{\hat{\Omega}} \boldsymbol{\epsilon}_{\mathrm{X}}[\boldsymbol{Y}] : \mathbf{E} : \hat{\boldsymbol{\epsilon}}[\boldsymbol{Y}^*]\; \mathrm{d}\hat{\Omega}, \tag{14c}$$

$$m_4(X,X^*) = \int_{I_{\mathrm{x}}} \frac{dX}{dx}\; \frac{dX^*}{dx}\; \mathrm{d}x, \qquad a_4(\boldsymbol{Y},\boldsymbol{Y}^*) = \int_{\hat{\Omega}} \boldsymbol{\epsilon}_{\mathrm{X}}[\boldsymbol{Y}] : \mathbf{E} : \boldsymbol{\epsilon}_{\mathrm{X}}[\boldsymbol{Y}^*]\; \mathrm{d}\hat{\Omega}. \tag{14d}$$

This allows for computing the integrals separately. This separation is however not possible for $l(\boldsymbol{Y}^*X^*)$

$$l(\boldsymbol{Y}^*X^*) = \int_{I_{\mathrm{x}}} \int_{\hat{\Gamma}_{\mathrm{N}}} \boldsymbol{t}(\boldsymbol{y},x) \cdot \boldsymbol{Y}^*\; X^*\;\; \mathrm{d}\hat{\Gamma}\; \mathrm{d}x, \tag{15}$$

because $\boldsymbol{t}(\boldsymbol{y}, x)$ depends on $\boldsymbol{y}$ and x in an inseparable way, cf. (4). The computation of this term is discussed in subsequent section and in Appendix A. Finally, (11) can be explicitly written as finding $X_N \in \mathbb{X}$ and $\boldsymbol{Y}_N \in \mathbb{Y}$ such that

$$\sum_{I=1}^{4} m_I(X_N, X_N)\ a_I(\boldsymbol{Y}_N, \delta\boldsymbol{Y}) = l(\delta\boldsymbol{Y} X_N) - \sum_{n=1}^{N-1}\sum_{I=1}^{4} m_I(\boldsymbol{X}_n, X_N) a_I(Y_n, \delta\boldsymbol{Y}) \quad \forall \delta\boldsymbol{Y} \in \mathbb{Y}, \tag{16a}$$

$$\sum_{I=1}^{4} m_I(X_N, \delta X)\ a_I(\boldsymbol{Y}_N, \boldsymbol{Y}_N) = l(\boldsymbol{Y}_N \delta X) - \sum_{n=1}^{N-1}\sum_{I=1}^{4} m_I(\boldsymbol{X}_n, \delta X) a_I(Y_n, \boldsymbol{Y}_N) \quad \forall \delta X \in \mathbb{X}. \tag{16b}$$

Here we can see that (16a) and (16b) describe the 2D and 1D problems, respectively.

3.2. Fixed-point algorithm for the YX-coupled problem

Since $\boldsymbol{Y}_N(\boldsymbol{y})$ and $X_N(x)$ appear in a coupled product, the problem is nonlinear and must be solved in a suitable iterative scheme. To solve the mode in the enrichment step N, we will adopt a fixed-point alternating algorithm so that ${\boldsymbol{Y}_N}^{(k)}$ can be computed in iteration k assuming that $X_N^{(k-1)}$ is known, then ${X_N}^{(k)}$ can be updated from ${\boldsymbol{Y}_N}^{(k)}$. This process is repeated until convergence is reached. Each iteration in the fixed-point algorithm consists of:

1. Compute ${\boldsymbol{Y}_N}^{(k)}$ from the previous out-of-plane mode $X_N^{(k-1)}$, where the weak form (11a) is approximated to find ${\boldsymbol{Y}_N}^{(k)} \in \mathbb{Y}$ such that
$$a({\boldsymbol{Y}_N}^{(k)}\ X_N^{(k-1)}, \delta\boldsymbol{Y} X_N^{(k-1)}) = l(\delta\boldsymbol{Y} X_N^{(k-1)}) - a(\boldsymbol{u}_{N-1}^{\mathrm{PGD}}, \delta\boldsymbol{Y} X_N^{(k-1)}) \quad \forall \delta\boldsymbol{Y} \in \mathbb{Y}. \tag{17}$$
2. Compute ${X_N}^{(k)}$ from the newly evaluated in-plane displacement mode ${\boldsymbol{Y}_N}^{(k)}$, whereby the weak form (11b) is approximated to find ${X_N}^{(k)} \in \mathbb{X}$ such that
$$a({\boldsymbol{Y}_N}^{(k)}\ {X_N}^{(k)}, {\boldsymbol{Y}_N}^{(k)}\ \delta X) = l({\boldsymbol{Y}_N}^{(k)}\ \delta X) - a(\boldsymbol{u}_{N-1}^{\mathrm{PGD}}, {\boldsymbol{Y}_N}^{(k)}\ \delta X) \quad \forall \delta X \in \mathbb{X}. \tag{18}$$

At each enrichment step, the initial guesses for $X_N^{(0)}(x)$ in the fixed point iteration are specified. In this paper, we initialized this in two ways: (1) with an arbitrary start guess and (2) with a start guess that has an orthogonal function concerning the previous normalized mode shapes. The 2nd start guess is a way to expand the solution domain since the direction of the mode shape is forced.

Each enrichment step requires multiple fixed-point iterations. The fixed point iterations continue until the weighted difference Δ between two iteration steps is smaller than a tolerance ϵ_{FP}, i.e., until

$$\Delta := \sqrt{|\Delta\alpha_N|^2 + \|\Delta\hat{\boldsymbol{Y}}_N\|_{\mathrm{Y}}^2 + \|\Delta\hat{X}_N\|_{\mathrm{X}}^2} < \epsilon_{\mathrm{FP}}. \tag{19}$$

Here, α_N and $\hat{\boldsymbol{Y}}_N$, $\hat{X}_N$ are the amplitude and the normalized mode shapes, respectively,

$$\alpha_N = \|\boldsymbol{Y}_N\|_{\mathrm{Y}}\ \|X_N\|_{\mathrm{X}}, \tag{20a}$$

$$\hat{\boldsymbol{Y}}_N = \frac{\boldsymbol{Y}_N}{\|\boldsymbol{Y}_N\|_{\mathrm{Y}}}, \quad \|\boldsymbol{Y}\|_{\mathrm{Y}} := \sqrt[4]{\sum_{I=1}^{4}[a_I(\boldsymbol{Y}, \boldsymbol{Y})]^2}, \tag{20b}$$

$$\hat{X}_N = \frac{X_N}{\|X_N\|_{\mathrm{X}}}, \quad \|X\|_{\mathrm{X}} := \sqrt[4]{\sum_{I=1}^{4}[m_I(X, X)]^2}. \tag{20c}$$

Here, the non-standard norms $\|\bullet\|_{\mathrm{Y}}$ and $\|\bullet\|_{\mathrm{X}}$ are chosen such that they provide an upper bound of the energy norm defined in (5) as follows:

$$\|\boldsymbol{Y}X\|_{\mathrm{a}} = \sqrt{\sum_{I=1}^{4} m_I(X, X) a_I(\boldsymbol{Y}, \boldsymbol{Y})} \leq \sqrt{\sqrt{\sum_{I=1}^{4}[m_I(X, X)]^2}\sqrt{\sum_{I=1}^{4}[a_I(\boldsymbol{Y}, \boldsymbol{Y})]^2}} = \|\boldsymbol{Y}\|_{\mathrm{Y}} \cdot \|X\|_{\mathrm{X}}, \tag{21}$$

for any product $\boldsymbol{Y}X$.

To compute Δ in (19) correctly, we first define the increment in the amplitude as $\Delta\alpha_N = {\alpha_N}^{(k)} - \alpha_N^{(k-1)}$. In order to deal with the ambiguity of signs for the normalized mode shapes, noting that $\hat{X}_N\hat{\boldsymbol{Y}}_N = (-\hat{X}_N)(-\hat{\boldsymbol{Y}}_N)$, the discrepancies $\Delta\hat{X}_N$ and $\Delta\hat{\boldsymbol{Y}}_N$ are defined as

$$\Delta\hat{X}_N = \gamma {\hat{X}_N}^{(k)} - \hat{X}_N^{(k-1)}, \quad \Delta\hat{\boldsymbol{Y}}_N = \gamma {\hat{\boldsymbol{Y}}_N}^{(k)} - \hat{\boldsymbol{Y}}_N^{(k-1)}, \tag{22}$$

where the sign shift is chosen as

$$\gamma = \arg \min_{\hat{\gamma} \in \{-1,1\}} \|\hat{\gamma} {\hat{X}_N}^{(k)} - \hat{X}_N^{(k-1)}\|. \tag{23}$$

The stopping criterion for the enrichment process is defined as

$$\frac{\alpha_N}{\alpha_1} < \epsilon, \tag{24}$$

when the ratio between the amplitude of mode N and the first mode becomes smaller than the tolerance ϵ or the desired amount of modes is obtained. Therefore, the computational cost is dominated by the total number of iterations of the 2D problem. The matrix structure of the problem is defined in Appendix A. A schematic illustration of the PGD algorithm for this separated representation can be seen in Fig. 2.

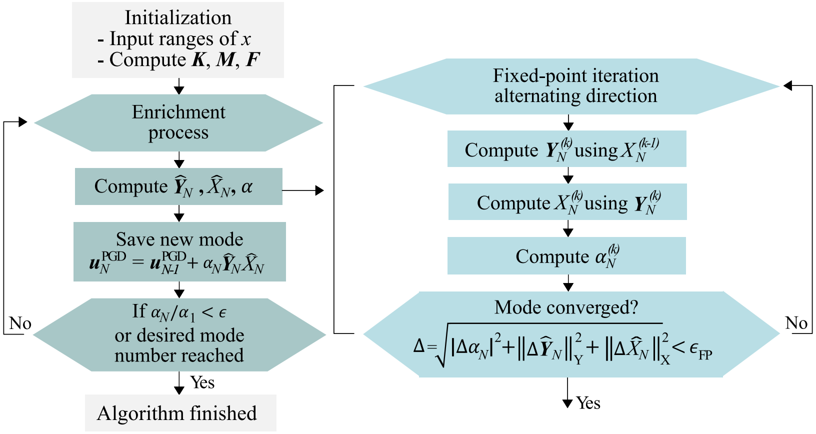

Fig. 2. The PGD algorithm for the in- and out-of-plane separated representation. The enrichment process continues until the stopping criterion is met, or the desired amount of modes is reached. The fixed-point iteration is conducted for k iterations in each enrichment step.

3.3. Verification against 3D FE simulation

To validate the accuracy of the PGD formulation and highlight the benefits when it comes to computational time and memory resources, we compare the PGD solution with a standard 3D FE solution for an equivalent discretization in- and out-of-plane, as shown in Fig. 3. The matrix structure of the 3D FE problem and its relation to the matrix definition of the PGD problem is explained in Appendix B.

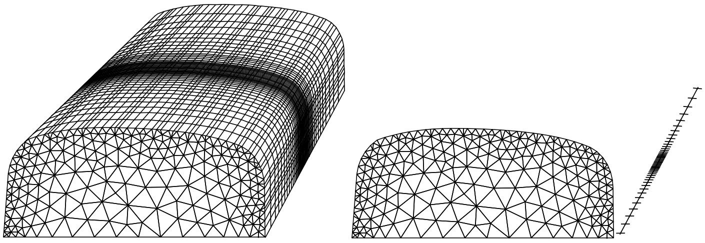

Fig. 3. Illustration of how the 3D rail head is modeled with 3D FE wedge elements. For the PGD solution, 2D linear elements are used in $\hat{\Omega}$, and 1D linear elements are used in I_x.

The 3D rail head has linear elastic material properties and a contact scenario prescribed with Hertz-distributed load in the elastic region. Table 1 describes the material parameters and load settings. The depth of the rail is set to $d = 100$ mm to approximate an infinite part of the rail.

Table 1
Input data of prescribed Hertz load shown in Fig. 1 for a contact scenario limited to the elastic region of the rail material.

Parameter		Value
Elastic modulus	E	210 GPa
Poisson's ratio	ν	0.3 [–]
Width, Depth	w, d	[70, 100] mm
Load position	s	10 mm
Semi-axes	a, b	[15, 10] mm
Normal surface contact traction	p_{n}	212 MPa
Lateral surface contact traction	p_{t}	21 MPa
Longitudinal surface contact traction	p_{x}	0 MPa

The 3D FE solution is performed using wedge elements for the discretization of $762\times 50 = 22\,860$ DOF. The discretization is refined close to the contact, both in- and out-of-plane, which is evident from Fig. 3. The PGD solution contains an equivalent discretization with 762 in-plane DOF composed of 3-noded triangular elements with linear shape functions and 50 out-of-plane DOF for 1D linear elements. Here, the spatial coordinate x may be regarded as a parameter for the X_N modes in the PGD approximation. In- and out-of-plane discretization was chosen to get accurate solutions while not having a computationally demanding 3D FE solution. Also, when more modes are added to the separated representation, the discretization should be able to capture higher-order mode forms.

3.3.1. Convergence

Although the PGD approach is an a priori method, the appropriate tolerance for the fixed-point iterations and enrichment process requires investigation for each specific problem.

To examine the impact of tolerance in the fixed-point algorithm, different values were assigned. A lower value on the tolerance results in a higher number of iterations, but does not necessarily improve the quality of the solution. Moreover, for specific enrichment steps, the stopping criterion (19) may not become smaller than the tolerance. Therefore, we set the maximum number of iterations at 20 and the tolerance at $\epsilon_{\mathrm{FP}} = 10^{-2}$.

The starting guesses X_N^0 provided to the fixed-point algorithm can impact the number of fixed-point iterations required. To investigate this, two different types of start guesses were used: (1) arbitrarily and (2) orthogonal start guesses. The arbitrary start guesses resulted in 115 total iterations on average to solve 10 modes. The start guesses that had an orthogonal function concerning the previous normalized mode shapes converged within 87 iterations. Additionally, the orthogonal start guesses were able to converge within the 20 iterations at each enrichment step, which is not the case for the arbitrarily chosen ones. However, it is important to note that the solution is not affected by the choice of the start guesses, but the orthogonal start guesses will be used due to the faster convergence of the fixed-point algorithm.

To investigate an acceptable tolerance for the enrichment process and assess the rate of convergence of the PGD solution, the relative error in energy norm e between the PGD and the reference 3D FE solution is computed as

$$e = \frac{\|\boldsymbol{u}_{\mathrm{FE}} - \boldsymbol{u}_{\mathrm{PGD}}\|_a}{\|\boldsymbol{u}_{\mathrm{FE}}\|_a}, \tag{25}$$

where the energy norm was defined in (5) and $\boldsymbol{u}_{\mathrm{PGD}}$ and $\boldsymbol{u}_{\mathrm{FE}}$ are the nodal displacements of the PGD and 3D FE solution, respectively. Fig. 4(a) shows the error as a function of the number of modes, while Fig. 4(b) shows the vertical displacement across the rail section for different numbers of modes included in the solution. As the number of terms included in the separated representation increases, the enriched solution gradually improves. However, the contribution of the first mode to the solution is more significant than that of the subsequent modes. At 15 modes and 160 total iterations, the solution achieves an acceptable accuracy of 0.2%, which should roughly correspond to the average von Mises stress error in the body. The maximum displacement error is 0.3%. At 15 modes, the ratio between the amplitudes (24) is less than $4\cdot 10^{-3}$, which is used as the tolerance for the enrichment loop when the discretization is changed in Section 3.3.4.

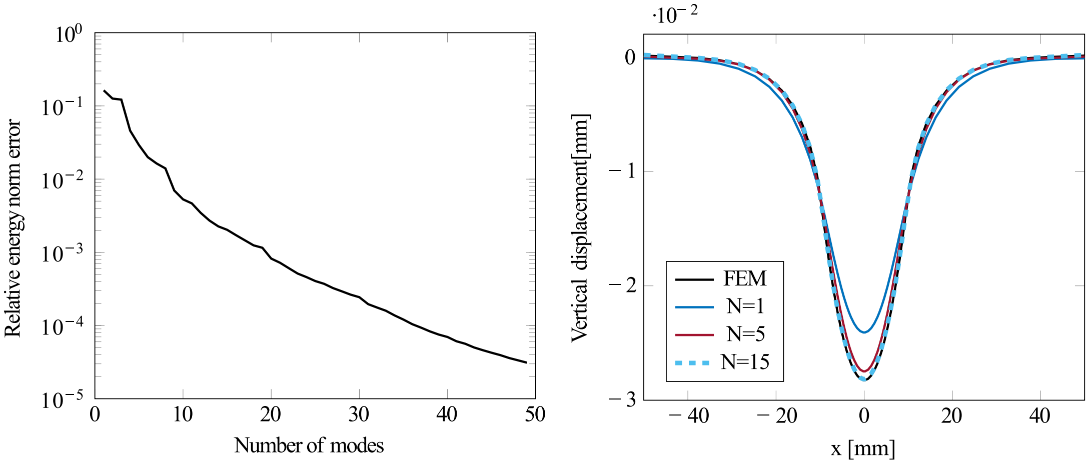

(a)

(b)

Fig. 4. (a) The number of modes is displayed against the relative energy norm error as defined in (25). (b) How the solution changes for an increasing amount of modes included in the solution. The solution has converged with only a few modes included in the PGD approximation.

3.3.2. Mode shapes

The PGD solution is constructed from a sum of N modes. Fig. 5 displays the first five normalized mode shapes of $\hat{X}_N$ and $\hat{\boldsymbol{Y}}_N$. It is worth noting that the first mode shape of $\hat{\boldsymbol{Y}}_N$ resembles the 2D solution obtained from standard 2D plane theories, while the other mode shapes $\hat{X}_N$ and $\hat{\boldsymbol{Y}}_N$ represent the 3D effects. It is emphasized that the in-plane mode $\boldsymbol{Y}_N$ is a vector field that contains both in-plane and out-of-plane displacement components along with the multiplicative correction X_N.

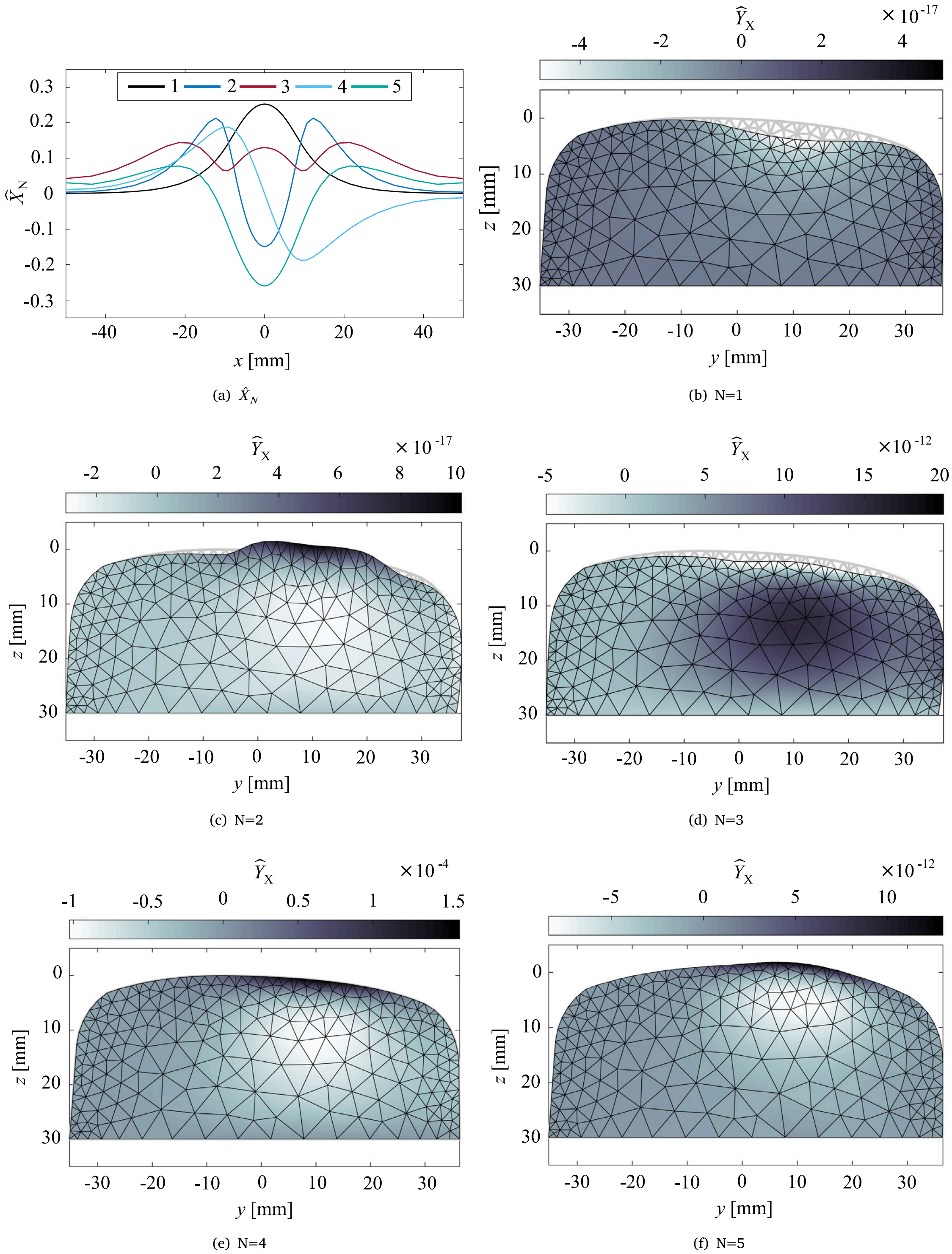

(a) $\hat{X}_N$

(b) N=1

(c) N=2

(d) N=3

(e) N=4

(f) N=5

Fig. 5. First five normalized mode shapes of (a) $\hat{X}_N$ and (b) $\hat{\boldsymbol{Y}}_N$. The gray color represents the local magnitudes of the out-of-plane component.

Additionally, the mode shapes 1, 2, 3 and 5 of X_n are symmetric around the x-axis, resulting in a very small out-of-plane component of $\hat{\boldsymbol{Y}}$, which is expected from the fact that the solution is symmetric about the $x = 0$ plane. However, the more significant 4th mode shape is nonsymmetric, corresponding to larger out-of-plane values for $\hat{\boldsymbol{Y}}$. As the number of modes increases, the order of the shape of the mode for $\hat{X}_N$ increases. Therefore, it is necessary to have a discretization with sufficiently small increments to capture higher-order mode forms.

3.3.3. von Mises stress

Fig. 6 shows the von Mises stress for a section of the rail and the error in the von Mises stress compared to the 3D FE solution for the converged solution. Stress is concentrated under the contact load, with a maximum value of 285 MPa, while the edges are nearly stress-free. The error in von Mises stress compared to the 3D FE solution is highest around the edges of the contact patch, reaching 6%, which is related to the discontinuity in the load. However, the average error in the body is about 0.4%, which is similar to the relative error in the energy norm discussed in Section 3.3.1. Hence, the PGD solution shows very promising results.

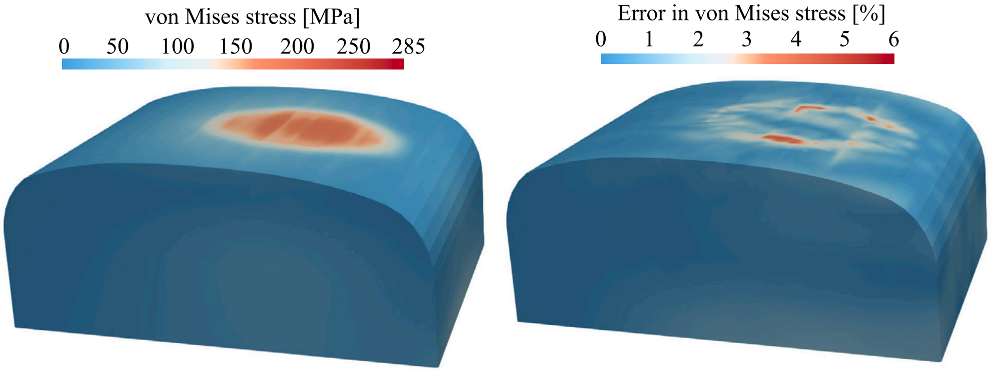

(a) (b)

Fig. 6. Illustration of the (a) von Mises stress and (b) the error in von Mises stress comparing the converged PGD solution to the 3D FE results.

3.3.4. CPU time and memory allocation

The PGD formulation offers a significant advantage in terms of the allocation of memory and time to the Central Processing Unit (CPU) compared to the 3D FE analysis as the Number of Degrees of Freedom (NDOF) increases. This is shown in Fig. 7, where the NDOF was changed in- and out-of-plane. For a small amount of DOF, the 3D FE analysis is slightly faster. As the NDOF increases, the CPU time increases rapidly, while the memory allocation increases linearly. In contrast, the CPU time of the PGD solution and the allocated memory remain nearly constant as the NDOF increases without compromising the accuracy of the solution. At the extreme corner, the PGD solution converges within 15 modes, with a relative error in the energy norm of 0.2%, while consuming only 3% of the CPU time and memory compared to the 3D FE solution.

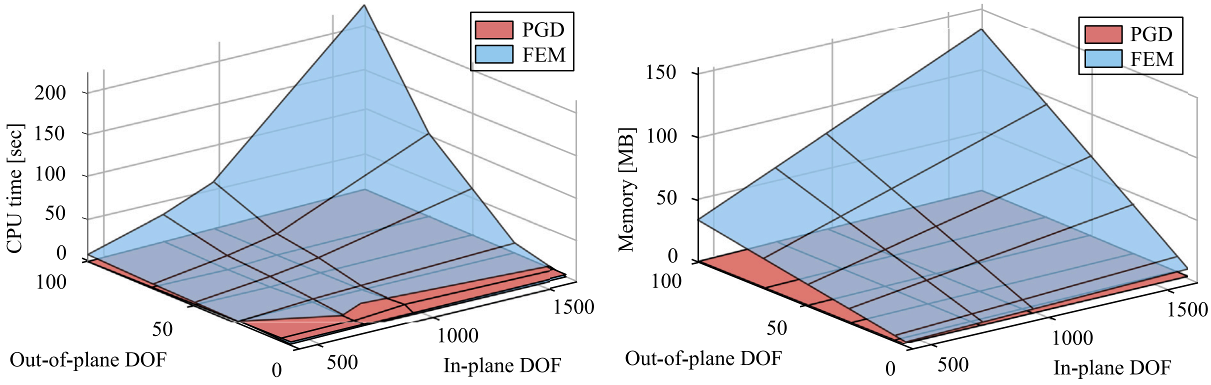

(a) (b)

Fig. 7. Comparisons of (a) CPU time and (b) memory allocation between PGD and 3D FE for different in- and out-of-plane discretizations.

The CPU time C for the 3D FE problem is proportional to the NDOF in the in-plane and out-of-plane directions, i.e., $C \propto [NDOF_{\mathrm{y}} \times NDOF_{\mathrm{x}}]^{\alpha}$. For the PGD approximation, the problem is solved instead for the total i iterations for the in-plane 2D problem and for the out-of-plane 1D problem, resulting in the relation $C \propto i \times [(NDOF_{\mathrm{y}})^{\alpha} + (NDOF_{\mathrm{x}})^{\alpha}]$. Therefore, the cost of the 1D problem is negligible compared to the 2D problem. This explains why there is not a significant increase in CPU time for the PGD solution even when the NDOF increases, since the number of modes and iterations required to represent the solution does not increase significantly.

4. 3D elastic PGD analysis of the rail for parameterized discrete load

In this section, we extend the analysis to find a parameterized solution in terms of a set of load parameters. The goal is to establish a PGD approximation that can be solved and stored from a calculation "offline" and then evaluated almost instantaneously in an "online" stage for a certain contact setup which would allow quick computations when many load scenarios are considered. In the studied case of linear elastic response, the load parameterization only affects the right-hand side, which makes PGD approach highly suitable. For greater generality, we shall consider a more complex loading situation than that described by the Hertzian load.

4.1. Semi-Hertzian contact using STRIPES

To address the distributed surface load, a discrete approach is taken for the contact stresses. The PGD formulation can accommodate extra coordinates since the extra dimension of the problem does not affect the solvability. Although a Hertzian contact load was initially applied, it may not be appropriate when the contact occurs at the flange corner of the wheel profile or when there are irregularities in the profiles of the contacting bodies, then the conformal contact and constant curvature assumptions of Hertz contact are violated [26]. Therefore, the semi-Hertzian approach called STRIPES, as described in [29,30], is used. This method discretizes the contact area parallel to the out-of-plane direction and locally determines the contact stresses in each strip by applying a Hertzian-based formula. The STRIPES approach allows for a more general load distribution, with non-constant lateral curvature and without assuming full slip. It also allows multiple contacts to be active simultaneously, and the separability of the load is greater than that with a Hertzian contact.

As shown in Fig. 8, the surface load in-plane is discretized with $m = [1, \ldots, M]$ parallel contact strips that act piecewise for a width of Δs. Each strip m has an assigned value for the maximum surface contact traction p^m_n, p^m_t and p^m_x applied in the corresponding normal ($\boldsymbol{e}^m_\mathrm{n}$), lateral ($\boldsymbol{e}^m_\mathrm{t}$) and longitudinal ($\boldsymbol{e}^m_\mathrm{x}$) direction to the rail profile at each strip.

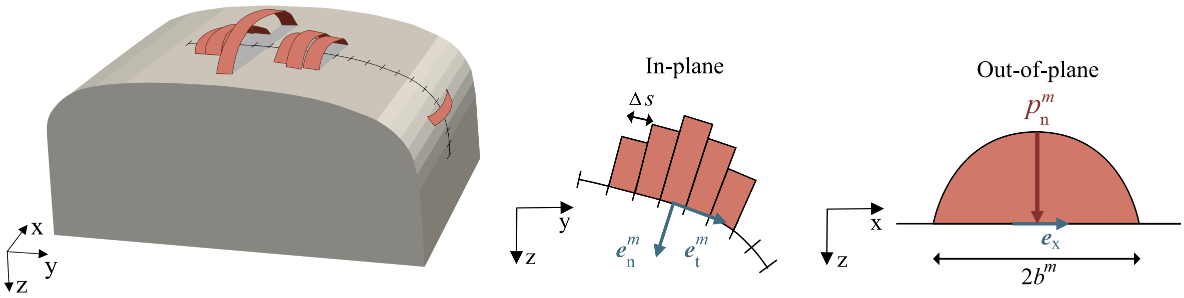

Fig. 8. Equivalent discrete load handling of the contact tractions. The contact traction is subdivided into a number of independent strips with the width Δs in-plane. Out-of-plane the load distribution is dictated parabolically defined as in (26).

Describing the contact load with STRIPES, there is a resemblance to Hertz's contact theory in (4) related to the out-of-plane direction, since the strips have the parabolic distribution $\rho(x, b^m)$ defined as

$$\rho(x, b^m) = \begin{cases} \sqrt{1 - \left(\frac{x}{b^m}\right)^2} & |x| < b^m, \\ 0 & |x| > b^m, \end{cases} \tag{26}$$

for the semi-axes b^m in each strip. With this load representation, the traction $\boldsymbol{t}$ is modeled as

$$\boldsymbol{t}(\boldsymbol{y}, x, \{b^m\}_m, \{p^m_\beta\}_{m,\beta}) = \sum_{m=1}^{M} \rho(x, b^m)\phi^m(\boldsymbol{y}) \sum_{\beta\in\mathbb{A}} p^m_\beta \; \boldsymbol{e}^m_\beta(\boldsymbol{y}), \tag{27}$$

where $\mathbb{A} = \{n, t, x\}$ are the indices for the normal n, lateral l, and longitudinal x direction and $\phi(\boldsymbol{y})$ is defined as

$$\phi^m(\boldsymbol{y}) = \begin{cases} 1 \text{ on } \hat{\Gamma}_m, \\ 0 \text{ else}, \end{cases} \tag{28}$$

where $\hat{\Gamma}_m$ is the surface on the rail of the active strip. Note that the discrete representation of the contact tractions makes the parameters separate for each strip. Also, surface contact tractions are completely separated within a strip. However, a relation between x and b^m remains due to the inseparable definition of $\rho(x, b^m)$ in (26).

4.2. The load-parameterized PGD approximation

Beyond the separated representation of the spatial coordinates $(\boldsymbol{y}, x)$ outlined in Section 3, the load parameters $\boldsymbol{p} = (\{b^m\}_m, \{p^m_\beta\}_{m,\beta})$ are parameterized. Therefore, we seek to determine an approximation of the parametric solution $\boldsymbol{u}(\boldsymbol{y}, x, \boldsymbol{p})$. The problem described in Section 2 is considered, but the loading follows from the traction $\boldsymbol{t}(\boldsymbol{p})$ defined in (27) as

$$l(\boldsymbol{p}; v) = \int_{I_{\mathrm{x}}} \int_{\hat{\Gamma}_{\mathrm{N}}} \boldsymbol{t}(\boldsymbol{p}) \cdot \boldsymbol{v} \, \mathrm{d}\hat{\Gamma} \, \mathrm{d}x. \tag{29}$$

The following sections describe how this can be done for a general ansatz and a linear ansatz by using the superposition of multiple PGD approximations for each strip.

4.2.1. General ansatz

For the general ansatz, we assume each parameter $b^m \in I_{\mathrm{b}}$ and $p^m_\beta \in I^\beta_{\mathrm{p}}$, where the intervals are the same for all strips m, to include the parameter space[3] $I_{\mathrm{p}} = [I_{\mathrm{b}}]^M \underset{\beta}{\times} [I^\beta_{\mathrm{p}}]^M$.

The hyper-dimensional weak form of the full problem reads as that of finding $\boldsymbol{u} \in \mathcal{U}$ such that

$$A(\boldsymbol{u}, \delta\boldsymbol{u}) = L(\delta\boldsymbol{u}) \quad \forall \delta\boldsymbol{u} \in \mathcal{U}, \tag{30}$$

with the bilinear and linear forms $A(\bullet, \bullet)$ and $L(\bullet)$ defined as

$$A(\boldsymbol{u}, \delta\boldsymbol{u}) = \int_{I_{\mathrm{p}}} a(\boldsymbol{u}, \delta\boldsymbol{u}) \, \mathrm{d}\boldsymbol{p}, \quad L(\delta\boldsymbol{u}) = \int_{I_{\mathrm{p}}} l(\boldsymbol{p}, \delta\boldsymbol{u}) \, \mathrm{d}\boldsymbol{p}, \tag{31}$$

representing the original problem as described in Section 2 integrated over the parameter domains $I_{\mathrm{p}} = [I_{\mathrm{b}}]^M \underset{\beta}{\times} [I^\beta_{\mathrm{p}}]^M$ with $\mathrm{d}\boldsymbol{p} = \left(\prod_m \mathrm{d}b^m\right)\left(\prod_{m,\beta} \mathrm{d}p^m_\beta\right)$.

The trial- and test-space describing functions pertinent to the weak form (30) reads

$$\mathcal{U} = \{\boldsymbol{v}(\boldsymbol{y}, x, \{b^m\}_m, \{p^m_\beta\}_{m,\beta}) : \int_{I_{\mathrm{p}}} \|\boldsymbol{v}(\bullet, \bullet, \{b^m\}_m, \{p^m_\beta\}_{m,\beta})\|^2_a \, \mathrm{d}\boldsymbol{p} < \infty, \boldsymbol{v} = \boldsymbol{0} \text{ on } \hat{\Gamma}_{\mathrm{d}}\}. \tag{32}$$

It becomes evident that, even in discretized form, the high dimensionality of the problem makes the explicit solution to (30) intractable in practice.

For the load parameterized problem, we shall now seek the PGD approximation of the displacement in the extended separated form to include the load parameters. This is formulated as

$$\boldsymbol{u}^{\mathrm{PGD}}_N(\boldsymbol{y}, x, \{b^m\}_m, \{p^m_\beta\}_{m,\beta}) = \sum_{n=1}^{N} \boldsymbol{Y}_n(\boldsymbol{y}) \; X_n(x) \prod_{m=1}^{M} B^m_n(b^m) \prod_\beta \; P^{m,\beta}_n(p^m_\beta), \tag{33}$$

where $b^m \in I_{\mathrm{b}}$ and $p^m_\beta \in I^\beta_{\mathrm{p}}$.

To set up the PGD problem of finding the Nth mode, the test function $\delta\boldsymbol{u}^{\mathrm{PGD}}$ can be written as

$$\begin{aligned} \delta\boldsymbol{u}^{\mathrm{PGD}}(\boldsymbol{y}, x, \{b^m\}_m, \{p^m_\beta\}_{m,\beta}) &= X_N \prod_m B^m_N \prod_\beta P^{m,\beta}_N \delta\boldsymbol{Y} + \boldsymbol{Y}_N \prod_m B^m_N \prod_\beta P^{m,\beta}_N \delta X \\ &+ \sum_{m=1}^{M} \boldsymbol{Y}_N X_N \left(\prod_{q\neq m} B^q_N\right)\left(\prod_{q,\beta} P^{q,\beta}_N\right) \delta B^m + \sum_{m=1}^{M} \sum_{\beta\in\mathbb{A}} \boldsymbol{Y}_N X_N \left(\prod_q B^q_N\right)\left(\prod_{\substack{q\neq m \\ \gamma\neq\beta}} P^{q,\gamma}_N\right) \delta P^{m,\beta} \end{aligned} \tag{34}$$

for variations $\delta\boldsymbol{Y},\ \delta X, \{\delta B^m\}_m,\ \{\delta P^{m,\beta}\}_{m,\beta} \in \mathbb{Y} \times \mathbb{X} \times [\mathbb{B}]^M \underset{\beta}{\times} [\mathbb{P}_\beta]^M$. Hence, we seek updates in the spaces $\mathbb{Y}$ and $\mathbb{X}$, defined in (10), and $\mathbb{B} = L_2(I_{\mathrm{b}})$, $\mathbb{P}_\beta = L_2(I^\beta_{\mathrm{p}})$. Here, $L_2(\bullet)$ denotes the space of square-integrable functions.

With the test function given above, we are now in a position to state the PGD problem for mode N in the expansion. The problem is then to find $\boldsymbol{Y}_N, X_N, \{B^m_N\}_m, \{\delta P^{m,\beta}_N\}_{m,\beta} \in \mathbb{Y} \times \mathbb{X} \times [\mathbb{B}]^M \underset{\beta}{\times} [\mathbb{P}_\beta]^M$ such that

$$A(\boldsymbol{Y}_N X_N \prod_m B^m_N \prod_\beta P^{m,\beta}_N, \delta\boldsymbol{u}^{\mathrm{PGD}}) = L(\delta\boldsymbol{u}^{\mathrm{PGD}}) - A(\boldsymbol{u}^{\mathrm{PGD}}_{N-1}, \delta\boldsymbol{u}^{\mathrm{PGD}}), \tag{35}$$

for any $\delta\boldsymbol{u}^{\mathrm{PGD}}$ on the form given in (34).

To solve the PGD approximation from (35) efficiently, we make use of the separation of the forms as

$$\sum_{I=1}^{4} F^{(Y)}_{I,N,N} a_I(\boldsymbol{Y}_N, \delta\boldsymbol{Y}) = \int_{\hat{\Gamma}_{\mathrm{N}}} \hat{\boldsymbol{t}}_N(\boldsymbol{y}) \cdot \delta\boldsymbol{Y} \, \mathrm{d}\hat{\Gamma} - \sum_{n=1}^{N-1} \sum_{I=1}^{4} F^{(Y)}_{I,N,n} a_I(\boldsymbol{Y}_n, \delta\boldsymbol{Y}) \quad \forall \delta\boldsymbol{Y} \in \mathbb{Y}, \tag{36a}$$

$$\sum_{I=1}^{4} F^{(X)}_{I,N,N} m_I(X_N, \delta X) = \int_{I_x} t_{x,N}(x) \delta X \, \mathrm{d}x - \sum_{n=1}^{N-1} \sum_{I=1}^{4} F^{(X)}_{I,N,n} m_I(X_n, \delta X) \quad \forall \delta X \in \mathbb{X}, \tag{36b}$$

$$F^{(B),m}_{N,N} m_b(B^m_N, \delta B^m) = \int_{I_b} g^m_N(b^m) \delta B^m \, \mathrm{d}b^m - \sum_{n=1}^{N-1} F^{(B),m}_{N,n} m_b(B^m_n, B^m_N) \quad \forall \delta B^m \in \mathbb{B},\ m \in \{1, \dots, M\}, \tag{36c}$$

---

[3] Here, we introduce the notation $\underset{\beta}{\times}$ for the product over all components $\beta \in \mathbb{A} = \{n, t, x\}$, i.e., $[I_{\mathrm{b}}]^M \underset{\beta}{\times} [I^\beta_{\mathrm{p}}]^M = [I_{\mathrm{b}}]^M \times [I^n_{\mathrm{p}}]^M \times [I^t_{\mathrm{p}}]^M \times [I^x_{\mathrm{p}}]^M$.

$$F^{(P),m,\beta}_{N,N} m^{\beta}_{p}(P^{m,\beta}_{N}, \delta P^{m,\beta}) = \int_{I^{\beta}_{p}} f^{m,\beta}_{0,N} + f^{m,\beta}_{1,N} p^{m}_{\beta} \delta P^{m,\beta} \ \mathrm{d}p^{m}_{\beta} - \sum_{n=1}^{N-1} F^{(P),m,\beta}_{N,n} m^{\beta}_{p}(P^{m,\beta}_{n}, P^{m,\beta}_{N}) \tag{36d}$$
$$\forall \delta P^{m,\beta} \in \mathbb{P}_{\beta},\ m, \beta \in \{1, \dots, M\} \times \mathbb{A}.$$

Here m_{I} and a_{I} defined in , whereas m_{b} and m_{p} are stated as

$$m_{\mathrm{b}}(B^m, B^{m*}) = \int_{I_{\mathrm{b}}} B^m \ B^{m*} \ \mathrm{d}b^m, \qquad m^{\mathrm{p}}_{\beta}(P^m_{\beta}, P^{m*}_{\beta}) = \int_{I^{\beta}_{\mathrm{p}}} P^m_{\beta} \ P^{m*}_{\beta} \ \mathrm{d}p^m_{\beta}. \tag{37}$$

In Appendix C, the detailed expressions for the components in Eqs. (36a)–(36d) can be found. It is important to note that all coefficients denoted by "F^{*}_{*}" are not affected by the mode of "its own" parameter. For example, $F^{(Y)}_{I,N,*}$ is independent of $\boldsymbol{Y}_N$ and $F^{(B),m}_{N,*}$ is independent of B^m_N.

The loading functions $\hat{\boldsymbol{t}}_N(\boldsymbol{y})$, $t_{x,N}(x)$ and $g^m_N(b^m)$ are in general nonlinear functions with respect to their respective parameters ($\boldsymbol{y}$, x and b^m), depending on the modes not solved for in the pertinent equation.[4] Therefore, the solutions $\boldsymbol{Y}_N(\boldsymbol{y})$, $X_N(x)$ and $B^m_N(b^m)$ are solved for (36a)–(36c). In practice, solutions are obtained numerically using the finite element method. However, considering (36d), we note that $f^{m,\beta}_{0,N}$ and $f^{m,\beta}_{1,N}$ are constants with respect to p^m_{β}, and define a linear loading term. As a result, the exact solution to the equation can be expressed explicitly in strong form as

$$P^{m,\beta}_{N}(p^m_{\beta}) = \frac{f^{m,\beta}_{0,N}}{F^{(P),m,\beta}_{N,N}} + \frac{f^{m,\beta}_{1,N}}{F^{(P),m,\beta}_{N,N}} p^m_{\beta} - \sum_{n=1}^{N-1} \frac{F^{(P),m,\beta}_{N,n}}{F^{(P),m,\beta}_{N,N}} P^{m,\beta}_{n}(p^m_{\beta}). \tag{38}$$

From induction, we see that $P^{m,\beta}_{N}$ will be linear for $N = 1, 2, \dots$. In conclusion, we seek discrete solutions using a fine discretization of the spaces $\mathbb{Y}$, $\mathbb{X}$, and $\mathbb{B}$. However, it is sufficient to represent linear functions in $\mathbb{P}_{\beta}$ to obtain the exact solution.

The problem is solved with the same fixed-point strategy explained in Section 3.1, but also including orthogonal start guesses for $B^{m,(0)}_{N}$ and $P^{m,\beta,(0)}_{N}$ at the beginning of each enrichment step. However, the stopping criteria for the fixed-point iterations (19) now also includes the difference between two iteration steps for the modes involving the load parameters

$$\varDelta = \sqrt{|\varDelta\alpha|^2 + \|\varDelta\hat{\boldsymbol{Y}}\|^2_{\mathrm{Y}} + \|\varDelta\hat{X}\|^2_{\mathrm{X}} + \sum_{m=1}^{M} \left(\|\varDelta\hat{\boldsymbol{B}}^m\|^2_{\mathrm{B}} + \sum_{\beta} \|\varDelta\hat{\boldsymbol{P}}^m_{\beta}\|^2_{\mathrm{P}} \right)} < \epsilon_{\mathrm{FP}}, \tag{39}$$

where ϵ_{FP} is the tolerance, and $\hat{\boldsymbol{B}}^m$ and $\hat{\boldsymbol{P}}^{m,\beta}$ are the normalized modes shapes. The amplitude α_N and norms $\|\bullet\|_{\mathrm{B}}$ and $\|\bullet\|_{\mathrm{P}}$ of the load parameters read

$$\alpha_N = \|\boldsymbol{Y}_N\|_{\mathrm{U}} \ \|X_N\|_{\mathrm{X}} \prod_{m=1}^{M} \|B^m_N\|_{\mathrm{B}} \prod_{\beta} \|P^m_{N,\beta}\|_{\mathrm{P}}, \qquad \|B\|_{\mathrm{B}} = \sqrt{\frac{1}{I_{\mathrm{b}}} m_{\mathrm{b}}(B, B)}, \qquad \|P_{\beta}\|_{\mathrm{P}} = \sqrt{\frac{1}{I^{\beta}_{\mathrm{p}}} m_{\mathrm{p}}(P_{\beta}, P_{\beta})}. \tag{40}$$

Each norm is divided by the length of the interval I_{b} and I^{β}_{p} to provide a numerically stable solution when the number of strips increases. Selecting the increment for the mode shapes $\varDelta\hat{\boldsymbol{Y}}$, $\varDelta\hat{X}$, $\varDelta\hat{\boldsymbol{B}}^m$ and $\varDelta\hat{\boldsymbol{P}}^m_{\beta}$ in (39) is computed similar to what was done in (22) and (23). When the solution is available, the displacement field can be generated for any configuration of the contact load within their respective intervals.

Remark. The detailed equations for the fixed-point iterations are omitted for brevity. They follow explicitly from the (nonlinear) PGD Eqs. (36a)–(36d) analogously to the fixed-point iterations (17) and (18) follow from (11) in Section 3. This means that the coefficients $F^{(*)}$, $f^{m,\beta}_{0,N}$, and $f^{m,\beta}_{1,N}$, and the functions $\hat{\boldsymbol{t}}_N(\boldsymbol{y})$, $t_{x,N}(x)$, and $g^m_N(b^m)$ will depend on various iterations of the modes N rather than the converged values. In particular, the fact that $P^{m,\beta}_{N}$ is linear will also hold for any iterative solution $P^{m,\beta(k)}_{N}$. □

4.2.2. Linear ansatz

From linearity, we can see that the solution to the weak form (2), with parameterized loading defined in (27) and (29), can be written on the form

$$\boldsymbol{u}(\boldsymbol{y}, x, \boldsymbol{p}) = \sum_{m=1}^{M} \sum_{\beta=1} \boldsymbol{u}^{m,\beta}(\boldsymbol{y}, x, b^m) \ p^m_{\beta}, \tag{41}$$

where the "sensitivity" fields can be solved as $\boldsymbol{u}^{m,\beta}(\boldsymbol{y}, x, b) \in \mathbb{U}$ such that

$$a(\boldsymbol{u}^{m,\beta}, \delta\boldsymbol{u}) = l^{m,\beta}(b; \delta\boldsymbol{u}) \quad \forall \delta\boldsymbol{u} \in \mathbb{U}. \tag{42}$$

Here, $l^{m,\beta}(\bullet;\bullet)$ for each strip m and direction β is defined as

$$l^{m,\beta}(b; \delta\boldsymbol{u}) = \int_{\varGamma_{\mathrm{N}}} \rho(x, b^m) \boldsymbol{e}_{\beta}(\boldsymbol{y}) \phi^m(\boldsymbol{y}) \delta\boldsymbol{u} \ \mathrm{d}\varGamma. \tag{43}$$

---

[4] $\hat{\boldsymbol{t}}_N(\boldsymbol{y})$ does not depend on $\boldsymbol{Y}_N$, $t_{x,N}(x)$ does not depend on X_N and $g^m_N(b^m)$ does not depend on B^m_N,

We shall now seek the PGD approximations of each sensitivity, i.e., for $m = [1, \ldots, M]$ and $\beta \in \mathbb{A}$, we approximate the displacement as

$$\boldsymbol{u}_N^{m,\beta,\mathrm{PGD}}(\boldsymbol{y}, x, b) = \sum_{n=1}^{N} \boldsymbol{Y}_n^{m,\beta}(\boldsymbol{y}) X_n^{m,\beta}(x) B_n^{m,\beta}(b). \tag{44}$$

We establish the hyper-dimensional weak form of (42) as finding $\boldsymbol{u}^{m,\beta}(\boldsymbol{y}, x, b) \in \mathcal{U}$ such that

$$\int_{I_\mathrm{b}} a(\boldsymbol{u}^{m,\beta}, \delta\boldsymbol{u})\,\mathrm{d}b = \int_{I_\mathrm{b}} l^{m,\beta}(b; \delta\boldsymbol{u})\,\mathrm{d}b \quad \forall \delta\boldsymbol{u} \in \mathcal{U}. \tag{45}$$

For this case, we define the trial and test space as $\mathcal{U} = \{\boldsymbol{u}(\boldsymbol{y}, x, b) : \int_{I_\mathrm{b}} \|\boldsymbol{u}\|_a^2\,\mathrm{d}b < \infty, \boldsymbol{u} = \boldsymbol{0} \text{ on } \hat{\Gamma}_\mathrm{d}\}$.

Using the separated representation of the spatial coordinates $(\boldsymbol{y}, x)$, and the parameter b, we may state the PGD problem of finding the modes $\boldsymbol{Y}_N^{m,\beta}$, $X_N^{m,\beta}$ and $B_N^{m,\beta}$ such that

$$m_\mathrm{b}(B_N^{m,\beta}, B_N^{m,\beta}) \sum_{I=1}^{4} m_I(X_N^{m,\beta}, X_N^{m,\beta})\; a_I(\boldsymbol{Y}_N^{m,\beta}, \delta\boldsymbol{Y}) = \int_{I_\mathrm{b}} B_N^{m,\beta}\, l^{m,\beta}(b, \delta\boldsymbol{Y} X_N^{m,\beta})\,\mathrm{d}b \tag{46a}$$

$$- \sum_{n=1}^{N-1} m_\mathrm{b}(B_n^{m,\beta}, B_N^{m,\beta}) \sum_{I=1}^{4} m_I(X_n^{m,\beta}, X_N^{m,\beta}) a_I(Y_n^{m,\beta}, \delta\boldsymbol{Y}) \quad \forall \delta\boldsymbol{Y} \in \mathbb{Y},$$

$$m_\mathrm{b}(B_N^{m,\beta}, B_N^{m,\beta}) \sum_{I=1}^{4} m_I(X_N^{m,\beta}, \delta X)\; a_I(\boldsymbol{Y}_N^{m,\beta}, \boldsymbol{Y}_N^{m,\beta}) = \int_{I_\mathrm{b}} B_N^{m,\beta}\, l^{m,\beta}(b, \boldsymbol{Y}_N^{m,\beta} \delta X)\,\mathrm{d}b \tag{46b}$$

$$- \sum_{n=1}^{N-1} m_\mathrm{b}(B_n^{m,\beta}, B_N^{m,\beta}) \sum_{I=1}^{4} m_I(X_n^{m,\beta}, \delta X) a_I(Y_n^{m,\beta}, \boldsymbol{Y}_N^{m,\beta}) \quad \forall \delta X \in \mathbb{X},$$

$$m_\mathrm{b}(B_N^{m,\beta}, \delta B) \sum_{I=1}^{4} m_I(X_N^{m,\beta}, X_N^{m,\beta})\; a_I(\boldsymbol{Y}_N^{m,\beta}, \boldsymbol{Y}_N^{m,\beta}) = \int_{I_\mathrm{b}} \delta B\, l^{m,\beta}(b, \boldsymbol{Y}_N^{m,\beta} X_N^{m,\beta})\,\mathrm{d}b \tag{46c}$$

$$- \sum_{n=1}^{N-1} m_\mathrm{b}(B_n^{m,\beta}, \delta B) \sum_{I=1}^{4} m_I(\boldsymbol{X}_n^{m,\beta}, X_N^{m,\beta}) a_I(Y_n^{m,\beta}, \boldsymbol{Y}_N^{m,\beta}) \quad \forall \delta B \in \mathbb{B}.$$

where m_I and a_I are defined in , m_b is defined in (37) and we recall $\mathbb{B} = L_2(I_\mathrm{b})$.

Finally, the approximation of the displacement field reads

$$\boldsymbol{u}(y, \boldsymbol{x}, \boldsymbol{p}) \approx \sum_{m=1}^{M} \sum_{\beta \in \mathbb{A}} \boldsymbol{u}_N^{m,\beta,\mathrm{PGD}}(\boldsymbol{y}, x, b^m)\; p_\beta^m. \tag{47}$$

The PGD approximations for each sensitivity are solved with the fixed point strategy explained in Section 3.1 including orthogonal start guesses for $B_N^{m,\beta}$ at the beginning of each enrichment step. The stopping criteria for the fixed-point iterations (19) is now defined as

$$\Delta = \sqrt{|\Delta\alpha|^2 + \|\Delta\hat{\boldsymbol{Y}}^{m,\beta}\|_{\mathbb{Y}}^2 + \|\Delta\hat{X}^{m,\beta}\|_{\mathbb{X}}^2 + \|\Delta\hat{B}^{m,\beta}\|_{\mathbb{B}}^2} < \epsilon_\mathrm{FP}, \tag{48a}$$

$$\alpha_N = \|\boldsymbol{Y}_N^{m,\beta}\|_{\mathbb{U}}\; \|X_N^{m,\beta}\|_{\mathbb{X}}\; \|B_N^{m,\beta}\|_{\mathbb{B}}, \quad \|B\|_{\mathbb{B}} = \sqrt{m_\mathrm{b}(B, B)}, \tag{48b}$$

and also includes the difference between two iteration steps for the modes $\hat{B}^{m,\beta}$ pertaining to the semi-axis. Selecting the increment for the mode shapes $\Delta\hat{\boldsymbol{Y}}^{m,\beta}$, $\Delta\hat{X}^{m,\beta}$ and $\Delta\hat{B}^{m,\beta}$ in (48a) is computed similar to what was done in (22) and (23).

4.3. Verification for different interpolated hertzian loads

In this Section, we will verify the PGD parameterization of the discrete load by comparing the resulting PGD formulations, presented in (33) and (47), to different reference 3D FE solutions for selected realizations of the load ($\boldsymbol{p}$). To generate relevant loading cases in the form given in (27), we choose parameters b^m and p_β^m that represent a piecewise constant approximation of a Hertzian load. Importantly, the reference FE solution will always correspond to the discrete traction form. The discretization for the meshes in- and out-of-plane is the same as that used in Section 3.3.

The reference Hertz load cases are obtained by placing the contact patch center at $s = 0$ mm and using a semi-axis of $a_\mathrm{H} = 10$ mm. Therefore, the strips will be discretized between $[-10, 10]$ mm, while varying the semi-axis b_H and the traction magnitudes. The discrete Hertzian semi-axis b^m and the surface contact traction magnitudes p_n^m, p_t^m, and p_x^m are determined through interpolation; see Fig. 9. We consider nine different samples of $b_\mathrm{H} = [6, 10, 14]$ mm and $p_{\mathrm{n,H}} = [75, 150, 225]$ MPa, as shown in Fig. 10(b). The lateral and longitudinal traction is set to 15% of the normal surface traction magnitude, pertinent to full-slip conditions.

For PGD formulations, the load parameters can vary within the ranges specified in Table 2. These intervals were determined based on different contact scenarios from the vehicle–track interaction generated from the load sequence described in [5]. The load magnitudes are limited to the elastic region of the rail material. Each parameter is discretized with a uniform 1D FE mesh of continuous linear elements, allowing the solution to be interpolated to any value within the intervals.

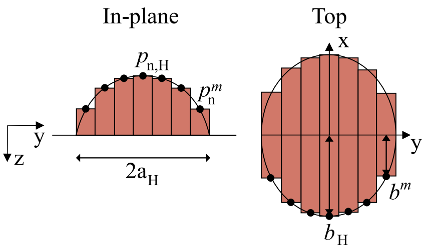

Fig. 9. The discrete load parameter b^m, p_{n}^m, p_{t}^m, p_{x}^m are identified through interpolation at the points marked with black circles for a theoretical Hertzian distribution, defined by parameters a_{H}, b_{H} and $p_{\mathrm{n,H}}$.

Table 2
Parameterized load for discrete contact strips. The intervals were found by generating the load sequence explained in [5]. The load magnitudes are limited to the elastic region of the rail material.

Parameter		Interval
Semi-axis	b	[0,16] mm
Normal surface contact traction	p_{n}	[0,300] MPa
Lateral surface contact traction	p_{t}	[−50, 50] MPa
Longitudinal surface contact traction	p_{x}	[−50, 50] MPa

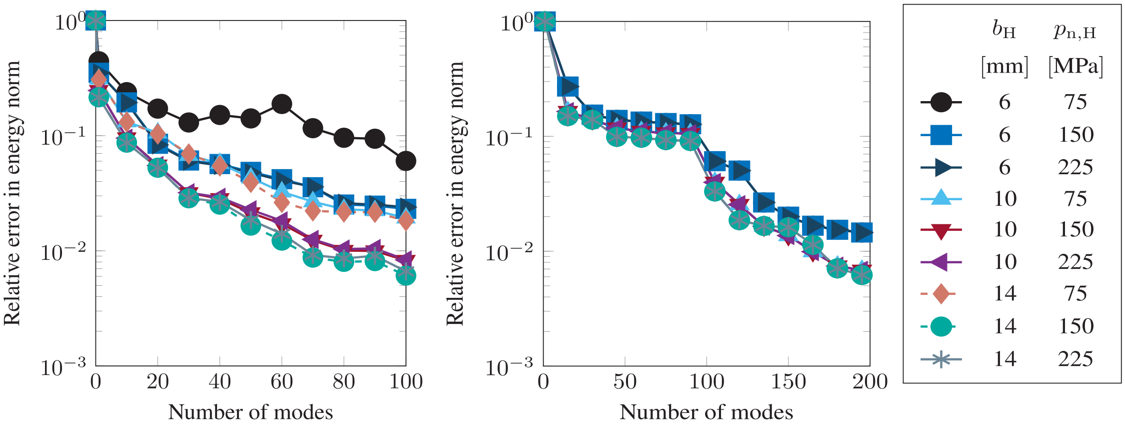

(a) General ansatz

(b) Linear ansatz

Fig. 10. The relative energy norm error for the PGD approximation compared to the 3D FE results shown against the number of modes for different interpolated Hertzian loads. The number of strips is M=5, and the PGD discretization of b^m pertains to 40 points. Results are shown for (a) the general and (b) the linear ansatz.

4.3.1. Discretization of load parameters and settings for fixed-point algorithm

For both PGD load formulations, we adopt a discretization with 40 points for the semi-axis, b^m, to provide a good balance between accuracy and computational cost. This resolution enables the representation of higher-order mode forms. For the general ansatz, the load amplitude p_{β}^m is discretized with two points since it is sufficient to employ only one linear element, as previously demonstrated in Section 4.2.1.

The accuracy of the PGD approximations for both load formulations varies in the parameter space, as seen in Fig. 10, where different solutions are displayed against the relative error in the energy norm defined in (25) for five strips. For the linear ansatz, the number of modes refers to the sum of all modes for all sensitivity fields. Also, the convergence is only affected by the choice of b_{H} since b^m is the only load parameter in the PGD approximations for the linear ansatz. The variation in convergence is greater for the general ansatz since the convergence is also affected by the choice of load magnitude. However, in all cases, the general trend is that the error decreases as more modes are included in the solution.

As explained in Section 3.3.1, the convergence depends on the tolerance specified for the fixed-point iteration. For the general ansatz, the tolerance is set to $\epsilon_{\mathrm{FP}} = 0.1$ accounting for the fact that Δ as defined in (39) scales with the number of parameters. As for the linear ansatz, the tolerance is the same as for the domain decomposition, $\epsilon_{\mathrm{FP}} = 10^{-2}$, since only one extra coordinate is treated. The order in which the parameters are solved within the fixed-point algorithm can also impact the number of iterations required for convergence, but that is not the case for this problem.

4.3.2. Influence of number of strips

To see how the number of strips M influences the results, the strips are distributed over the area of the contact patch. The number of strips is limited by the in-plane mesh size. The width of the strips Δs cannot be smaller than the largest distance between the nodes on the upper edge within the contact patch region. For the in-plane discretization, the largest width is about 2.3 mm on the upper edge. Thus, with the selected semi-axis value $a_{\mathrm{H}} = 10$ mm, a maximum of eight strips can be applied.

The impact of the number of strips M on convergence is shown in Fig. 11. The Root Mean Square Error (RMSE) is computed as

$$\mathrm{RMSE} = \sqrt{\frac{\sum_{i=1}^{N_{\mathrm{load}}} \|\boldsymbol{u}_{\mathrm{FE}}(\boldsymbol{p}_i) - \boldsymbol{u}_{\mathrm{PGD}}(\boldsymbol{p}_i)\|_a^2}{\sum_{i=1}^{N_{\mathrm{load}}} \|\boldsymbol{u}_{\mathrm{FE}}(\boldsymbol{p}_i)\|_a^2}}, \tag{49}$$

where the energy norm was defined in (5), and $\boldsymbol{u}_{\mathrm{PGD}}$ and $\boldsymbol{u}_{\mathrm{FE}}$ are the nodal displacements of the PGD and 3D FE solution for load scenario $\boldsymbol{p}_i$ with N_{load} load scenarios considered. As the number of strips increases, more values are treated as coordinates for the general ansatz, or more PGD solutions are included for the linear ansatz. As a result, the solution becomes more complex, and the convergence decreases. Thus, more modes must be included to reach the same accuracy when more strips are considered. This is also evident from Fig. 13(a), which shows the total number of modes necessary to include for different amounts of strips to reach a RMSE of 1%.

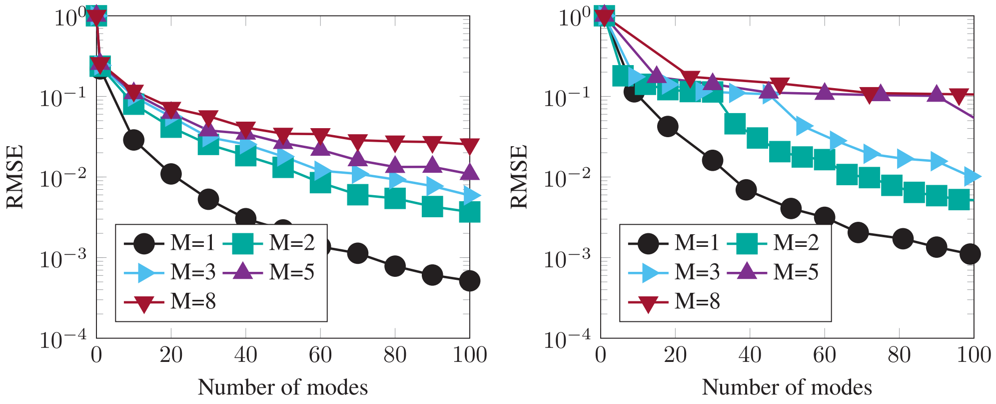

(a) General ansatz

(b) Linear ansatz

Fig. 11. Influence of the number of strips M on the RMSE as defined in (49) for the case of using approximately 100 modes. Results are shown for (a) the general and (b) the linear ansatz.

Comparing the results for the different PGD implementations of the load, the convergence is similar (cf. Figs. 11 and 13). However, to achieve the same level of accuracy, the linear ansatz requires a few more modes, this becomes evident as the number of strips increases. On the other hand, this comes at a much lower offline computational cost, see Figs. 12 and 13(b). Fig. 12 displays the CPU time at 100 modes, while Fig. 13(b) shows the CPU time versus the number of strips when the solution has reached the RMSE of 1%. It is evident that the linear ansatz, despite requiring a larger number of modes, offers greater computational efficiency. This is due to the fact that the sum $\boldsymbol{u}_{N-1}^{\mathrm{PGD}}$ requires more computations when more factors are incorporated into each term of the sum, thus increasing the solution time employing the general ansatz. On the contrary, the linear ansatz features fewer factors in each term of the sum as outlined in (44) and (46), resulting in a reduced computational cost.

4.4. Result of applying a semi-Hertzian contact

So far, the solution has been validated by assuming a Hertzian load distribution. However, one of the advantages of the discrete contact approach is its flexibility when it comes to variations in the shape of the contact area in the lateral direction and variations in the magnitude of the load. Additionally, the approach allows for the simultaneous application of multiple contact points. To demonstrate these advantages, 20 strips were applied throughout the loaded region $[-15, 35]$ mm on the top surface, found from the generated load sequence [5]. The load parameters vary within the ranges specified in Table 2. The discretization for the in-plane and out-of-plane meshes is the same as that used in Section 3.3.

Nine representative load scenarios were generated using the commercial software Simpack v.2022, based on the load sequence described in [5]. In Simpack, the discrete elastic contact model was used, which employs the STRIPES method outlined in [29,30]. The contact model in Simpack acts similarly to how the load is parameterized in the PGD model. However, in Simpack, the width of the strips is 0.5 mm, whereas the strips generated from the PGD model are 2.5 mm wide.[5] As a result, the input to the PGD model consists of the average values for the load parameters obtained from five strips. One of the nine load cases is illustrated in Fig. 15, where each load parameter is normalized by $\hat{b}^m = b^m/|I_{\mathrm{b}}|$ and $\hat{p}_\beta^m = p_\beta^m/|I_{\mathrm{p}}^\beta|$ for their respective interval length, as given in Table 2.

---

[5] This is to guarantee the strips are wider than the largest distance of 2.3 mm between the in-plane nodes on the upper edge within the loaded region

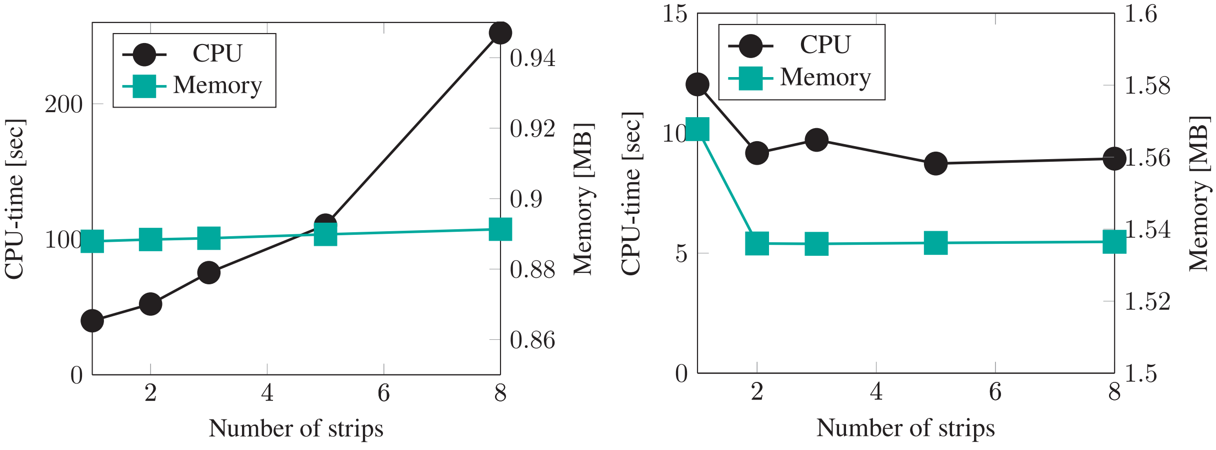

(a) General ansatz (b) Linear ansatz

Fig. 12. Influence of the number of strips M on the CPU time, and memory allocation for the case of using approximately 100 modes. Results are shown for (a) the general and (b) the linear ansatz.

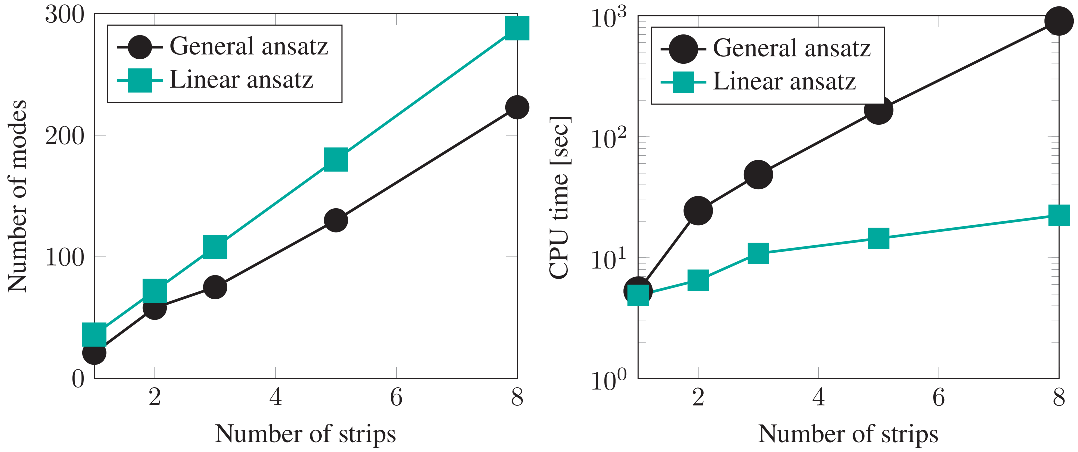

(a) (b)

Fig. 13. Total (a) number of modes and (b) CPU time required to reach 1% RMSE accuracy for the general and linear ansatz.

4.4.1. Convergence — influence of invariant parameters

Compared to the Hertz contact load discussed in Section 4.3, some strips are unloaded in the discrete load setup, as shown in Figs. 8 and 15. For a strip m, where $p_n^m = p_t^m = p_x^m = 0$, it is evident from the traction format in (27) that b^m cannot influence the exact solution. In fact, for the load scenario studied and the pertinent reference FE solution, no value for b^m is available for these strips. Using the linear ansatz, it also becomes clear from (47) that b^m does not affect the approximation when $p_n^m = p_t^m = p_x^m = 0$. However, this invariance is not explicitly apparent in the PGD approximation for the general ansatz. Hence, we *have to* assign a value for b^m to all strips even though the traction component is zero.

In the following, we shall investigate two approaches for selecting b^m for those strips m on which no load p_β^m acts:

$$B_n^m(b^m) \leftarrow \begin{cases} B_n^m(\tilde{b}) \text{ or,} \\ \frac{1}{I_\text{b}} \int_{I_\text{b}} B_n^m(b^m)\ \mathrm{d}b^m, \end{cases} \qquad \forall m \in \{q :\ p_\beta^q = 0\} \quad \forall \beta \in \mathbb{A}, \tag{50}$$

for all modes $n = 1, \dots, N$. Thus, the two alternatives are either to set the parameter to a preset default $\tilde{b}$ or to integrate the average mode over the interval.

Fig. 14(a) displays the RMSE for the PGD approximations for both load formulations as a function of the number of modes. For the general ansatz, different strategies have been adopted for $B_n^m(b^m)$ as explained in (50). The evaluation is performed for nine load scenarios and the results are compared with the 3D FE solution. The Figure clearly shows that, unlike the exact solution, the PGD solution of the general ansatz is not invariant to the values of b^m. Thus, the accuracy of the PGD solution is sensitive to the adopted strategy.

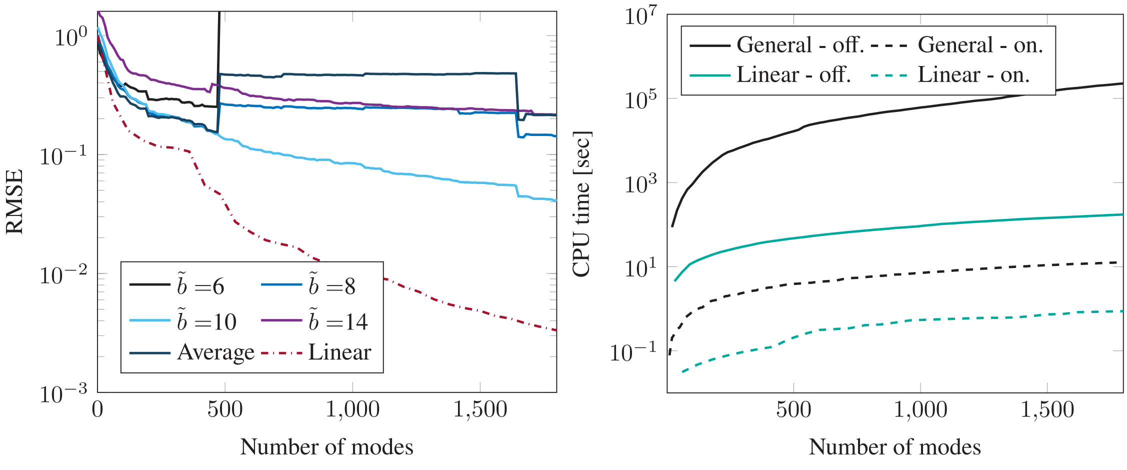

Fig. 14. (a) RMSE for the PGD approximation compared to 3D FE solutions for nine different load scenarios. For the general ansatz, the RMSE value is shown for different values on $b = \tilde{b}$ for the unloaded strips. In one case ("Average"), the mode contribution is averaged. For the linear ansatz ("Linear"), inactive strips are eliminated explicitly and no strategy needs to be selected. (b) Offline ("off".) and online ("on".) CPU cost for the general and linear ansatz.

In Fig. 14(a), it appears that the solution cannot converge when a small value of $\tilde{b}$ is assigned to the unloaded strips ($\tilde{b} = 6$ mm). This behavior may be related to the relationship between the semi-axis and the out-of-plane coordinate x. When $\tilde{b}$ is small, more X modes are needed to obtain an accurate solution. In contrast, setting the value too high ($\tilde{b} = 14$ mm) will also result in lower accuracy. By averaging the mode contributions, or when $\tilde{b} = 8$ mm, the solution initially converges, but the accuracy deteriorates after 475 modes, but improves after mode 1646. The most accurate solution is approximately in the middle of the interval, for $\tilde{b} = 10$ mm. However, the convergence of the adopted strategy for $B_n^m(b^m)$ depends on the reference solution. The PGD approximation of the linear ansatz is not sensitive to the invariance and has much better convergence. At 1800 modes, the RMSE is 0.33% for the linear ansatz compared to 4.11% RMSE for the general ansatz when $\tilde{b} = 10$ mm.

Fig. 14(b) displays the CPU time against the total number of modes to compute the PGD approximation, which can be done at an "off-line" stage. Furthermore, to exemplify the online cost, the time required to construct the (3D) displacement field for a given load setup is shown for the two procedures. At 1800 modes, it takes 12.83 s to generate the displacement vector for the general ansatz, whereas it takes 0.88 s for the linear ansatz.

4.4.2. von Mises stress for one load scenario

As an example, Fig. 15 shows the load parameters on each strip for one of the nine load scenarios evaluated in Section 4.4.1. The Figure shows that three different contact points are active, that the contact area is no longer elliptical, and that the traction in-plane

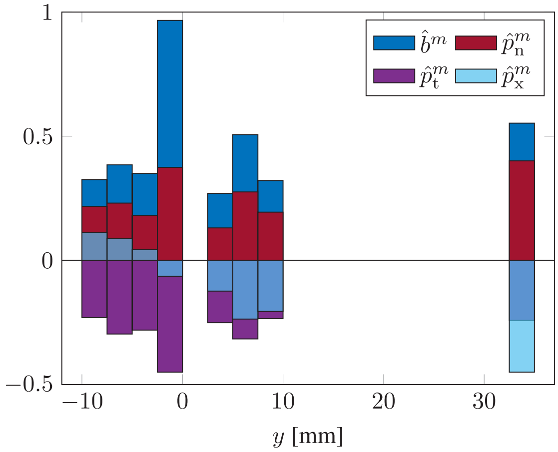

Fig. 15. Given load parameters for each strip m for a sample load scenario. The loading scenario consists of three different contact points and in total eight active strips out of 20 total strips. Each load parameter is normalized for its respective interval length given in Table 2.

of the surface contact is no longer parabolic. Additionally, each load parameter is normalized by scaling it with its corresponding interval length given in Table 2, i.e., $\hat{b}^m = b^m/|I_\mathrm{b}|$ and $\hat{p}^m_\beta = p^m_\beta/|I^\beta_\mathrm{p}|$.

For the given load scenario, the linear ansatz-based PGD approximation exhibits a relative error of 0.35% for the energy norm and an error of 0.84% for the maximum displacement in 1800 modes. Fig. 16 displays the von Mises stress and the error of the von Mises stress compared to the 3D FE solution for this loading scenario. The maximum von Mises stress for the PGD solution is 269 MPa, while the reference has the highest von Mises stress at 264 MPa. Therefore, the PGD solution slightly overestimates the stresses in the rail head, resulting in a maximum error of 4.8%. However, the accuracy of the von Mises stress is fairly low throughout the body. Increasing the number of modes in the solution would further reduce the error.

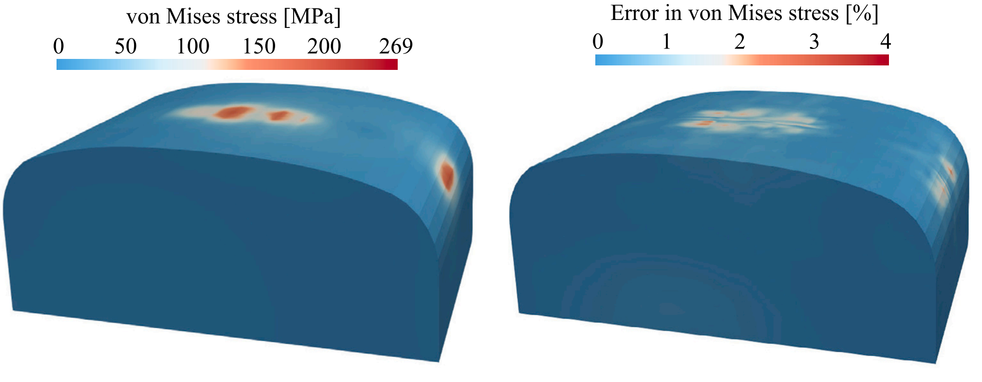

(a) (b)

Fig. 16. Illustration of the (a) von Mises stress and (b) the error in von Mises stress comparing the PGD solution for the linear ansatz to the 3D FE results for the load scenario displayed in Fig. 15.

5. Conclusions

In this paper, a Proper Generalized Decomposition (PGD) formulation is proposed to efficiently solve various contact scenarios in a three-dimensional elastic rail head. First, the spatial domain is separated into a two-dimensional in-plane discretization of the rail cross-section and a one-dimensional out-of-plane discretization, which constitutes parameters in the PGD approximation. Comparing the PGD approximation with a three-dimensional finite element solution with the same discretization demonstrates high accuracy of the PGD approximation, measured as the relative error in the energy norm. This formulation offers significant computational cost reduction and memory allocation savings, making it suitable for fast online simulations under specific loads.

The second part of the paper focuses on extending the PGD formulation to address a parametric problem encompassing a wide range of contact scenarios. To model these scenarios, we employ the semi-Hertzian contact approach STRIPES which employs a distributed load characterized by piecewise constant in-plane and parabolic out-of-plane properties for a specific strip width. This approach enables a separate representation of the traction, accommodating different variations in contact shape and magnitude distribution, as well as the presence of multiple active contact points. The discrete load is parameterized in two ways; based on a general and linear ansatz.

In the general ansatz, the load parameters, including the out-of-plane semi-axes (b^m) and the traction magnitudes (p^m_n, p^m_t, p^m_x) in the normal, lateral, and longitudinal directions, for each strip m, are treated as extra coordinates within their intervals. This PGD formulation handles the load in a general, high-dimensional format, considering numerous variables.

Alternatively, in the linear ansatz, we take explicit advantage of the linearity of the problem and treat each strip in each loading direction as a separate PGD problem, introducing b^m as an extra coordinate. This allows us to combine different PGD solutions through superposition to generate the displacement field for any load case.

Both the general and linear ansatz show similar convergence behavior concerning the number of modes included in the solution. As more strips are incorporated, the complexity increases due to the increased number of parameters being treated as coordinates in the general ansatz or the need for additional PGD approximations in the linear ansatz. Consequently, more modes are required to accurately capture the loading setup. In terms of computational time, the linear ansatz is much more efficient than the general ansatz for both the offline and online stages. This allows for better scalability, both when it comes to increasing the number of modes and the number of strips. In cases where the exact solution is invariant for a given parameter, the PGD implementation of the linear ansatz performs better by avoiding the introduction of spurious dependencies for the unloaded strips.

The PGD approximation of the domain decomposition combined with the parameterized load computed during the offline stage encompasses all solutions for the three-dimensional displacement field of the load parameters within their respective intervals. This means that in the online stage, the solution can be obtained quickly as a postprocessing step of the precomputed parametric solution for many different load scenarios. An extension to include a constant curve radius could be considered in the model by using a curved-linear coordinate system. For applications involving wheel–rail contacts, the inclusion of an elastic–plastic material becomes necessary to investigate to capture damage mechanisms such as accumulated plastic deformation. In this development, efficient load parameterization is of particular importance.

Declaration of competing interest

The authors declare that they have no known competing financial interests or personal relationships that could have appeared to influence the work reported in this paper.

Data availability

No data was used for the research described in the article.

Acknowledgments

The current study is part of the ongoing activities at CHARMEC — Chalmers Railway Mechanics (www.chalmers.se/charmec). Parts of the study have been funded by the European Union's Horizon 2020 research and innovation program in the In2Track3 under grant agreement No. 101012456, and the authors would like to thank the Swedish Transport Administration (Trafikverket) for their support. Some of the computations were enabled by resources provided by the National Academic Infrastructure for Supercomputing in Sweden (NAISS) at Chalmers Centre for Computational Science and Engineering (C3SE) partially funded by the Swedish Research Council through a grant agreement No. 2022-06725.

Appendix A. Matrix structure of the separated representation

The weak forms of the PGD approximation (17) and (18) can be rewritten to matrix form by employing (linear) finite elements. The FE-subspaces are introduced as $\mathbb{Y}_h \subset \mathbb{Y}$ and $\mathbb{X}_h \subset \mathbb{X}$, where the spaces were defined in (10). The nodal approximations for $\boldsymbol{Y}_N(\boldsymbol{y})$ and $X_N(x)$ with the $\boldsymbol{N}^{(\mathrm{y})}(\boldsymbol{y})$ and $N^{(\mathrm{x})}(x)$ are FE shape functions read

$$\boldsymbol{Y}_N(\boldsymbol{y}) \approx \sum_{i=1}^{NDOF_{\mathrm{y}}} \boldsymbol{N}_i^{(\mathrm{y})}(\boldsymbol{y})(\underline{\boldsymbol{Y}}_N)_i \in \mathbb{Y}_h, \qquad \delta\boldsymbol{Y}(\boldsymbol{y}) \approx \sum_{i=1}^{NDOF_{\mathrm{y}}} \boldsymbol{N}_i^{(\mathrm{y})}(\boldsymbol{y})(\delta\underline{\boldsymbol{Y}})_i, \tag{A.1a}$$

$$X_N(x) \approx \sum_{i=1}^{NDOF_{\mathrm{x}}} N_i^{(\mathrm{x})}(x)(\underline{\boldsymbol{X}}_N)_i \in \mathbb{X}_h, \qquad \delta X(x) \approx \sum_{i=1}^{NDOF_{\mathrm{x}}} N_i^{(\mathrm{x})}(x)(\delta\underline{\boldsymbol{X}})_i \tag{A.1b}$$

$$\frac{dX_N(x)}{dx} \approx \sum_{i=1}^{NDOF_{\mathrm{x}}} B_i(x)(\underline{\boldsymbol{X}}_N)_i \in \mathbb{X}_h, \qquad \frac{d\delta X(x)}{dx} \approx \sum_{i=1}^{NDOF_{\mathrm{x}}} B_i(x)(\delta\underline{\boldsymbol{X}})_i, \tag{A.1c}$$

where vectors $\underline{\boldsymbol{Y}}_N$ and $\underline{\boldsymbol{X}}_N$ contain nodal values in the FE mesh of the in- and out-of-plane parameters, respectively, whereas $\delta\underline{\boldsymbol{Y}}$ and $\delta\underline{\boldsymbol{X}}$ contain the corresponding arbitrary parameters. The sum goes to the NDOF of each parameter. The corresponding FE-approximations of the strains (12) are

$$\hat{\boldsymbol{\epsilon}}[\boldsymbol{Y}_N(\boldsymbol{y})] \approx \sum_{i=1}^{NDOF_{\mathrm{y}}} \hat{\boldsymbol{\epsilon}}[\boldsymbol{N}_i^{(\mathrm{y})}(\boldsymbol{y})](\underline{\boldsymbol{Y}}_N)_i = \sum_{i=1}^{NDOF_{\mathrm{y}}} \boldsymbol{B}_i^{(\Omega)}(\boldsymbol{y})(\underline{\boldsymbol{Y}}_N)_i, \qquad \hat{\boldsymbol{\epsilon}}[\delta\boldsymbol{Y}(\boldsymbol{y})] \approx \sum_{i=1}^{NDOF_{\mathrm{y}}} \boldsymbol{B}_i^{(\Omega)}(\boldsymbol{y})(\delta\underline{\boldsymbol{Y}})_i, \tag{A.2a}$$

$$\boldsymbol{\epsilon}_{\mathrm{X}}[\boldsymbol{Y}_N(\boldsymbol{y})] \approx \sum_{i=1}^{NDOF_{\mathrm{y}}} \boldsymbol{\epsilon}_{\mathrm{X}}[\boldsymbol{N}_i^{(\mathrm{y})}(\boldsymbol{y})](\underline{\boldsymbol{Y}}_N)_i = \sum_{i=1}^{NDOF_{\mathrm{y}}} \boldsymbol{B}_i^{(\mathrm{x})}(\boldsymbol{y})(\underline{\boldsymbol{Y}}_N)_i \qquad \boldsymbol{\epsilon}_{\mathrm{X}}[\delta\boldsymbol{Y}(\boldsymbol{y})] \approx \sum_{i=1}^{NDOF_{\mathrm{y}}} \boldsymbol{B}_i^{(\mathrm{x})}(\boldsymbol{y})(\delta\underline{\boldsymbol{Y}})_i. \tag{A.2b}$$

Using the FE-approximations (A.1) and (A.2) in the fixed-point algorithm (17) and (18) results in the discrete form of the problem

$$\tilde{a}(\underline{\boldsymbol{Y}}_N\ \underline{\boldsymbol{X}}_N, \delta\underline{\boldsymbol{Y}}\ \underline{\boldsymbol{X}}_N) = [\underline{\boldsymbol{X}}_N]^{\mathrm{T}}\underline{\boldsymbol{F}}\ \delta\underline{\boldsymbol{Y}} - \sum_{n=1}^{N-1} A(\underline{\boldsymbol{Y}}_n\ \underline{\boldsymbol{X}}_n, \delta\underline{\boldsymbol{Y}}\ \underline{\boldsymbol{X}}_N), \tag{A.3a}$$

$$\tilde{a}(\underline{\boldsymbol{Y}}_N\ \underline{\boldsymbol{X}}_N, \underline{\boldsymbol{Y}}_N\ \delta\underline{\boldsymbol{X}}) = [\delta\underline{\boldsymbol{X}}]^{\mathrm{T}}\underline{\boldsymbol{F}}\ \underline{\boldsymbol{Y}}_N - \sum_{n=1}^{N-1} \tilde{a}(\underline{\boldsymbol{Y}}_n\ \underline{\boldsymbol{X}}_n, \underline{\boldsymbol{Y}}_N\ \delta\underline{\boldsymbol{X}}), \tag{A.3b}$$

where the FE-discretized bilinear form $\tilde{a}(\bullet,\bullet)$ from (13) is defined as

$$\begin{aligned}\tilde{a}(\underline{\boldsymbol{Y}}\ \underline{\boldsymbol{X}}, \underline{\boldsymbol{Y}}^*\ \underline{\boldsymbol{X}}^*) =& \left([\underline{\boldsymbol{X}}^*]^{\mathrm{T}}\underline{\boldsymbol{M}}_{\Omega}\ \underline{\boldsymbol{X}}\right)\left([\underline{\boldsymbol{Y}}^*]^{\mathrm{T}}\underline{\boldsymbol{K}}_{\Omega}\ \underline{\boldsymbol{Y}}\right) + \left([\underline{\boldsymbol{X}}^*]^{\mathrm{T}}\underline{\boldsymbol{M}}_{\Omega\mathrm{X}}\ \underline{\boldsymbol{X}}\right)\left([\underline{\boldsymbol{Y}}^*]^{\mathrm{T}}\underline{\boldsymbol{K}}_{\Omega\mathrm{X}}\ \underline{\boldsymbol{Y}}\right)\\ &+ \left([\underline{\boldsymbol{X}}]^{\mathrm{T}}\underline{\boldsymbol{M}}_{\mathrm{X}\Omega}\ \underline{\boldsymbol{X}}^*\right)\left([\underline{\boldsymbol{Y}}^*]^{\mathrm{T}}\underline{\boldsymbol{K}}_{\mathrm{X}\Omega}\ \underline{\boldsymbol{Y}}\right) + \left([\underline{\boldsymbol{X}}]^{\mathrm{T}}\underline{\boldsymbol{M}}_{\mathrm{X}}\ \underline{\boldsymbol{X}}^*\right)\left([\underline{\boldsymbol{Y}}^*]^{\mathrm{T}}\underline{\boldsymbol{K}}_{\mathrm{X}}\ \underline{\boldsymbol{Y}}\right).\end{aligned} \tag{A.4}$$

The global stiffness matrices $\underline{\boldsymbol{K}}$, mass matrices $\underline{\boldsymbol{M}}$ and external force matrix $\underline{\boldsymbol{F}}$ reads

$$(\underline{\boldsymbol{K}}_{\Omega})_{kl} = \int_{\hat{\Omega}} \boldsymbol{B}_k^{(\Omega)}(\boldsymbol{y}) : \mathbf{E} : \boldsymbol{B}_l^{(\Omega)}(\boldsymbol{y})\ \mathrm{d}\hat{\Omega}, \qquad (\underline{\boldsymbol{M}}_{\Omega})_{kl} = \int_{I_{\mathrm{x}}} N_k^{(\mathrm{x})}(x) \cdot N_l^{(\mathrm{x})}(x)\ \mathrm{d}x, \tag{A.5a}$$

$$(\underline{\boldsymbol{K}}_{\Omega\mathrm{X}})_{kl} = \int_{\hat{\Omega}} \boldsymbol{B}_k^{(\Omega)}(\boldsymbol{y}) : \mathbf{E} : \boldsymbol{B}_l^{(\mathrm{x})}(\boldsymbol{y})\ \mathrm{d}\hat{\Omega}, \qquad (\underline{\boldsymbol{M}}_{\Omega\mathrm{X}})_{kl} = \int_{I_{\mathrm{x}}} B_k(x) \cdot N_l^{(\mathrm{x})}(x)\ \mathrm{d}x, \tag{A.5b}$$

$$(\underline{\boldsymbol{K}}_{\mathrm{X}\Omega})_{kl} = (\underline{\boldsymbol{K}}_{\Omega\mathrm{X}})_{lk}, \qquad (\underline{\boldsymbol{M}}_{\mathrm{X}\Omega})_{kl} = (\underline{\boldsymbol{M}}_{\Omega\mathrm{X}})_{lk} \tag{A.5c}$$

$$(\underline{\boldsymbol{K}}_{\mathrm{X}})_{kl} = \int_{\hat{\Omega}} \boldsymbol{B}_k^{(\mathrm{x})}(\boldsymbol{y}) : \mathsf{E} : \boldsymbol{B}_l^{(\mathrm{x})}(\boldsymbol{y}) \ \mathrm{d}\hat{\Omega}, \qquad (\underline{\boldsymbol{M}}_{\mathrm{X}})_{kl} = \int_{I_{\mathrm{x}}} B_k(x) \cdot B_l(x) \ \mathrm{d}x, \tag{A.5d}$$

$$(\underline{\boldsymbol{F}})_{kl} = \int_{I_{\mathrm{x}}} \int_{\hat{\Gamma}_{\mathrm{N}}} N_k^{(\mathrm{x})}(x) \boldsymbol{N}_l^{(\mathrm{y})}(\boldsymbol{y}) \cdot \boldsymbol{t} \ \mathrm{d}\hat{\Gamma} \ \mathrm{d}x. \tag{A.5e}$$

The advantage of the matrix structure of the problem is that $\underline{\boldsymbol{K}}$, $\underline{\boldsymbol{M}}$ and $\underline{\boldsymbol{F}}$ only need to be computed once. The FE-discrete form of the nodal displacements $\boldsymbol{u}_N^{\mathrm{PGD}}$ read

$$\boldsymbol{u}_N^{\mathrm{PGD}} = \sum_{n=1}^{N} \alpha_n \ \underline{\hat{\boldsymbol{Y}}}_n \ \underline{\hat{\boldsymbol{X}}}_n, \tag{A.6}$$

where α and $\underline{\hat{\boldsymbol{Y}}}$, $\underline{\hat{\boldsymbol{X}}}$ are the amplitude and normalized mode shapes, respectively, defined from .

Appendix B. Matrix structure of 3D FE solution

Taking advantage of the separated representation of the displacements and strain in the PGD formulation, the 3D FE approximations are defined as

$$\boldsymbol{u}(\boldsymbol{y}, x) \approx \sum_{n=1}^{NDOF_{\mathrm{x}}} \sum_{k=1}^{NDOF_{\mathrm{y}}} \boldsymbol{N}_k^{(\mathrm{y})}(\boldsymbol{y}) (\underline{\boldsymbol{u}}_n)_k \ N_n^{(\mathrm{x})}(x), \qquad \delta\boldsymbol{u}(\boldsymbol{y}, x) \approx \sum_{n=1}^{NDOF_{\mathrm{x}}} \sum_{k=1}^{NDOF_{\mathrm{y}}} \boldsymbol{N}_k^{(\mathrm{y})}(\boldsymbol{y}) (\delta\underline{\boldsymbol{u}}_N)_k \ N_n^{(\mathrm{x})}(x). \tag{B.7}$$

where $\underline{\boldsymbol{u}}$ are the nodal displacements whereas $\delta\underline{\boldsymbol{u}}$ is the corresponding arbitrary parameter. $\boldsymbol{N}_i^{(\mathrm{y})}(\boldsymbol{y})$ and $N_i^{(\mathrm{x})}(x)$ are the FE shape functions that was first defined in . The same separation of the strain (12) is used for the 3D FE, where the discrete form of the strains reads

$$\hat{\epsilon}[\boldsymbol{u}(\boldsymbol{y}, x)] \approx \sum_{n=1}^{NDOF_{\mathrm{x}}} \sum_{k=1}^{NDOF_{\mathrm{y}}} \hat{\epsilon}[\boldsymbol{N}_i^{(\mathrm{y})}(\boldsymbol{y})](\underline{\boldsymbol{u}}_n)_k \ N_n^{(\mathrm{x})}(x) = \sum_{n=1}^{NDOF_{\mathrm{x}}} \sum_{k=1}^{NDOF_{\mathrm{y}}} \boldsymbol{B}_i^{(\Omega)}(\boldsymbol{y}) \ (\underline{\boldsymbol{u}}_n)_k \ N_n^{(\mathrm{x})}(x), \tag{B.8a}$$

$$\hat{\epsilon}[\delta\boldsymbol{u}(\boldsymbol{y}, x)] \approx \sum_{n=1}^{NDOF_{\mathrm{x}}} \sum_{k=1}^{NDOF_{\mathrm{y}}} \boldsymbol{B}_i^{(\Omega)}(\boldsymbol{y})(\delta\underline{\boldsymbol{u}}_n)_k \ N_n^{(\mathrm{x})}(x), \tag{B.8b}$$

$$\epsilon_{\mathrm{X}}[\boldsymbol{u}(\boldsymbol{y}, x)] \approx \sum_{n=1}^{NDOF_{\mathrm{x}}} \sum_{k=1}^{NDOF_{\mathrm{y}}} \epsilon_{\mathrm{X}}[\boldsymbol{N}_i^{(\mathrm{y})}(\boldsymbol{y})](\underline{\boldsymbol{u}}_n)_k \ N_n^{(\mathrm{x})}(x) = \sum_{n=1}^{NDOF_{\mathrm{x}}} \sum_{k=1}^{NDOF_{\mathrm{y}}} \boldsymbol{B}_i^{(\mathrm{x})}(\boldsymbol{y})(\underline{\boldsymbol{u}}_n)_k \ N_n^{(\mathrm{x})}(x), \tag{B.8c}$$

$$\epsilon_{\mathrm{X}}[\delta\boldsymbol{u}(\boldsymbol{y}, x)] \approx \sum_{n=1}^{NDOF_{\mathrm{x}}} \sum_{k=1}^{NDOF_{\mathrm{y}}} \boldsymbol{B}_i^{(\mathrm{x})}(\boldsymbol{y})(\delta\underline{\boldsymbol{u}}_n)_k \ N_n^{(\mathrm{x})}(x). \tag{B.8d}$$

For these FE approximations, the FE-discrete form of the problem reads

$$\sum_{n=1}^{NDOF_{\mathrm{x}}} \delta\underline{\boldsymbol{u}}_n \ \underline{\boldsymbol{K}}_{nm} \ \underline{\boldsymbol{u}}_m = \sum_{n=1}^{NDOF_{\mathrm{x}}} \delta\underline{\boldsymbol{u}}_n \ \underline{\boldsymbol{f}}_n, \tag{B.9}$$

where the external force vector $\underline{\boldsymbol{f}}_n$, which is the nth column of $\underline{\boldsymbol{F}}$, and the global stiffness matrix $\underline{\boldsymbol{K}}_{nm}$ are defined as

$$(\underline{\boldsymbol{f}}_n)_k = \int_{I_{\mathrm{x}}} \int_{\hat{\Gamma}_{\mathrm{N}}} N_n^{(\mathrm{x})}(x) \boldsymbol{N}_k^{(\mathrm{y})}(\boldsymbol{y}) \cdot \boldsymbol{t} \ \mathrm{d}\hat{\Gamma} \ \mathrm{d}x, \tag{B.10a}$$

$$\underline{\boldsymbol{K}}_{nm} = (\underline{\boldsymbol{M}}_{\Omega})_{nm} \ \underline{\boldsymbol{K}}_{\Omega} + (\underline{\boldsymbol{M}}_{\Omega\mathrm{X}})_{nm} \ \underline{\boldsymbol{K}}_{\Omega X} + (\underline{\boldsymbol{M}}_{\mathrm{X}\Omega})_{nm} \ \underline{\boldsymbol{K}}_{X\Omega} + (\underline{\boldsymbol{M}}_{\mathrm{X}})_{nm} \ \underline{\boldsymbol{K}}_{\mathrm{X}}, \tag{B.10b}$$

here the separated representations of $\underline{\boldsymbol{K}}$ and $\underline{\boldsymbol{M}}$ are used and where defined in . It should be noted that $\underline{\boldsymbol{K}}_{nm} = \underline{\boldsymbol{0}}$ for $|m - n| > 1$. Thus, the problem in matrix form is written as

$$\begin{bmatrix} \underline{\boldsymbol{K}}_{11} & \underline{\boldsymbol{K}}_{12} & \underline{\boldsymbol{0}} & \cdots & \underline{\boldsymbol{0}} \\ \underline{\boldsymbol{K}}_{21} & \underline{\boldsymbol{K}}_{22} & \underline{\boldsymbol{K}}_{23} & \cdots & \underline{\boldsymbol{0}} \\ \cdots & \cdots & \cdots & \cdots & \cdots \\ \underline{\boldsymbol{0}} & \cdots & \cdots & \underline{\boldsymbol{K}}_{NDOF_{\mathrm{x}}-1,NDOF_{\mathrm{x}}-1} & \underline{\boldsymbol{K}}_{NDOF_{\mathrm{x}}-1,NDOF_{\mathrm{x}}} \\ \underline{\boldsymbol{0}} & \cdots & \cdots & \underline{\boldsymbol{K}}_{NDOF_{\mathrm{x}},NDOF_{\mathrm{x}}-1} & \underline{\boldsymbol{K}}_{NDOF_{\mathrm{x}},NDOF_{\mathrm{x}}} \end{bmatrix} \begin{bmatrix} u_1 \\ u_2 \\ \cdots \\ u_{NDOF_{\mathrm{x}}-1} \\ u_{NDOF_{\mathrm{x}}} \end{bmatrix} = \begin{bmatrix} \underline{\boldsymbol{f}}_1 \\ \underline{\boldsymbol{f}}_2 \\ \cdots \\ \underline{\boldsymbol{f}}_{NDOF_{\mathrm{x}}-1} \\ \underline{\boldsymbol{f}}_{NDOF_{\mathrm{x}}} \end{bmatrix}, \tag{B.11}$$

where $NDOF_{\mathrm{x}}$ is the NDOF out-of-plane.

Appendix C. Separated representation of load-parameterization

In order to solve the PGD approximation from (35) efficiently, we make use of the separation of variables. The separated representation of the bilinear and linear forms $A(\bullet, \bullet)$ and $L(\bullet)$ reads

$$A(\boldsymbol{Y} X \prod_m B^m \prod_{m,\beta} P^{m,\beta}, \boldsymbol{Y}^* \ X^* \prod_m B^{m*} \prod_{m,\beta} P^{m,\beta*}) = \sum_{I=1}^{4} m_I(X, X^*) \ a_I(\boldsymbol{Y}, \boldsymbol{Y}^*) \prod_m m_{\mathrm{b}}(B^m, B^{m*}) \prod_{m,\beta} m_{\mathrm{p}}^{\beta}(P^{m,\beta}, P^{m,\beta*}), \tag{C.12a}$$

$$
\begin{aligned}
L(\boldsymbol{Y}^* X^* \prod_m B^{m*} \prod_{m,\beta} P^{m,\beta*}) = \sum_{m=1}^{M} \sum_{\beta\in\mathbb{A}} \int_{I_\mathrm{b}} \int_{I_\mathrm{x}} \rho(x,b^m)\ X^*\ B^{m*}\ \mathrm{d}x\ \mathrm{d}b^m \times \cdots \\
\ldots \times \int_{I_\mathrm{p}^\beta} p_\beta^m\ P^{m,\beta*}\ \mathrm{d}p_\beta^m \int_{\hat{\Gamma}_\mathrm{N}} \phi^m(\boldsymbol{y})\ \boldsymbol{e}_\beta^m(\boldsymbol{y}) \cdot \boldsymbol{Y}^*\ \mathrm{d}\hat{\Gamma} \prod_{q\neq m} \int_{I_\mathrm{b}} B^{q*}\ \mathrm{d}b^q \prod_{\substack{q\neq m\\ \gamma\neq\beta}} \int_{I_\mathrm{p}^\gamma} P_\gamma^{q,\gamma*}\ \mathrm{d}p_\gamma^q,
\end{aligned} \tag{C.12b}
$$

with m_I and a_I defined in and m_b and m_p stated in (37).

Using the separation of the forms, we repeat (36) for completeness and seek $\boldsymbol{Y}_N, X_, \{B_N^m\}_m, \{\delta P_N^{m,\beta}\}_{m,\beta} \in \mathbb{Y}\times\mathbb{X}\times[\mathbb{B}]^M \underset{\beta}{\times} [\mathbb{P}_\beta]^M$ such that

$$
\sum_{I=1}^{4} F_{I,N,N}^{(\boldsymbol{Y})} a_I(\boldsymbol{Y}_N, \delta\boldsymbol{Y}) = \int_{\hat{\Gamma}_\mathrm{N}} \hat{\boldsymbol{t}}_N(\boldsymbol{y}) \cdot \delta\boldsymbol{Y}\ \mathrm{d}\hat{\Gamma} - \sum_{n=1}^{N-1} \sum_{I=1}^{4} F_{I,N,n}^{(\boldsymbol{Y})} a_I(\boldsymbol{Y}_n, \delta\boldsymbol{Y}) \quad \forall\delta\boldsymbol{Y}\in\mathbb{Y}, \tag{C.13a}
$$

$$
\sum_{I=1}^{4} F_{I,N,N}^{(X)} m_I(X_N, \delta X) = \int_{I_x} t_{x,N}(x)\delta X\ \mathrm{d}x - \sum_{n=1}^{N-1} \sum_{I=1}^{4} F_{I,N,n}^{(X)} m_I(X_n, \delta X) \quad \forall\delta X\in\mathbb{X}, \tag{C.13b}
$$

$$
F_{N,N}^{(B),m} m_b(B_N^m, \delta B^m) = \int_{I_b} g_N^m(b^m)\delta B^m\ \mathrm{d}b^m - \sum_{n=1}^{N-1} F_{N,n}^{(B),m} m_b(B_n^m, \delta B^m) \qquad \forall\delta B^m\in\mathbb{B},\ m\in\{1,\ldots,M\}, \tag{C.13c}
$$

$$
\begin{aligned}
F_{N,N}^{(P),m,\beta} m_p^\beta(P_N^{m,\beta}, \delta P^{m,\beta}) = \int_{I_p^\beta} f_{0,N}^{m,\beta} + f_{1,N}^{m,\beta} p_\beta^m \delta P^{m,\beta}\ \mathrm{d}p_\beta^m - \sum_{n=1}^{N-1} F_{N,n}^{(P),m,\beta} m_p^\beta(P_n^{m,\beta}, \delta P^{m,\beta}) \\
\forall\delta P^{m,\beta}\in\mathbb{P}_\beta,\ m,\beta\in\{1,\ldots,M\}\times\mathbb{A},
\end{aligned} \tag{C.13d}
$$

where “F_*^*” are independent of the corresponding mode and are defined as

$$
F_{I,N,N^*}^{(\boldsymbol{Y})} = m_I(X_{N^*}, X_N) \prod_m m_b(B_{N^*}^m, B_N^m) \prod_\beta m_p(P_{N^*}^{m,\beta}, P_N^{m,\beta}), \tag{C.14a}
$$

$$
F_{I,N,N^*}^{(\boldsymbol{X})} = a_I(\boldsymbol{Y}_{N^*}, \boldsymbol{Y}_N) \prod_m m_b(B_{N^*}^m, B_N^m) \prod_\beta m_p(P_{N^*}^{m,\beta}, P_N^{m,\beta}), \tag{C.14b}
$$

$$
F_{N,N^*}^{(B),m} = \sum_{I=1}^{4} a_I(\boldsymbol{Y}_{N^*}, \boldsymbol{Y}_N)\ m_I(X_{N^*}, X_N) \prod_{q\neq m} m_b(B_{N^*}^q, B_N^q) \prod_{q,\beta} m_p^\beta(P_{N^*}^{q,\beta}, P_N^{q,\beta}), \tag{C.14c}
$$

$$
F_{N,N^*}^{(P),m,\beta} = \sum_{I=1}^{4} a_I(\boldsymbol{Y}_{N^*}, \boldsymbol{Y}_N)\ m_I(X_{N^*}, X_N) \prod_q m_b(B_{N^*}^q, B_N^q) \prod_{q,\gamma\neq m,\beta} m_p^\gamma(P_{N^*}^{q,\gamma}, P_N^{q,\gamma}). \tag{C.14d}
$$

Furthermore, the loading terms become

$$
\hat{\boldsymbol{t}}_N(\boldsymbol{y}) = \sum_{m=1}^{M} \sum_{\beta\in\mathbb{A}} \hat{t}_N^{m,\beta} \phi^m(\boldsymbol{y}) \boldsymbol{e}_\beta^m(\boldsymbol{y}), \tag{C.15a}
$$

$$
\hat{t}_N^{m,\beta} = \int_{I_\mathrm{b}} \int_{I_\mathrm{x}} \rho(x,b^m)\ X_N\ B_N^m\ \mathrm{d}x\ \mathrm{d}b^m \int_{I_\mathrm{p}^\beta} p_\beta^m\ P_N^{m,\beta}\ \mathrm{d}p_\beta^m \prod_{q\neq m} \int_{I_\mathrm{b}} B_N^q\ \mathrm{d}b^q \prod_{\substack{q\neq m\\ \gamma\neq\beta}} \int_{I_\mathrm{p}^\gamma} P_N^{q,\gamma}\ \mathrm{d}p_\gamma^q, \tag{C.15b}
$$

$$
t_{x,N}(x) = \sum_{m=1}^{M} \sum_{\beta\in\mathbb{A}} t_{x,N}^{m,\beta} \int_{I_\mathrm{b}} \rho(x,b^m)\ B_N^m\ \mathrm{d}b^m, \tag{C.15c}
$$

$$
t_{x,N}^{m,\beta} = \int_{\hat{\Gamma}_\mathrm{N}} \phi^m(\boldsymbol{y}) \boldsymbol{e}_\beta^m(\boldsymbol{y}) \cdot \boldsymbol{Y}_N\ \mathrm{d}\hat{\Gamma} \int_{I_\mathrm{p}^\beta} p_\beta^m\ P_N^{m,\beta}\ \mathrm{d}p_\beta^m \prod_{q\neq m} \int_{I_\mathrm{b}} B_N^q\ \mathrm{d}b^q \prod_{\substack{q\neq m\\ \gamma\neq\beta}} \int_{I_\mathrm{p}^\gamma} P_N^{q,\gamma}\ \mathrm{d}p_\gamma^q, \tag{C.15d}
$$

$$
g_N^m(b^m) = g_{N,0}^m + G_N^m \int_{I_x} \rho(x,b^m) X_N\ \mathrm{d}x, \tag{C.15e}
$$

$$
g_{N,0}^m = \sum_{q\neq m} \sum_{\beta\in\mathbb{A}} \int_{\hat{\Gamma}_\mathrm{N}} \phi^q(\boldsymbol{y}) \boldsymbol{e}_\beta^q(\boldsymbol{y}) \cdot \boldsymbol{Y}_N\ \mathrm{d}\hat{\Gamma} \int_{I_p^\beta} p_\beta^q P_N^{q,\beta} \mathrm{d}p_\beta^q \prod_{r\neq\{m,q\}} \int_{I_\mathrm{b}} B_N^r \mathrm{d}b^r \prod_{\substack{r\neq q\\ \gamma\neq\beta}} \int_{I_\mathrm{p}^\gamma} P_N^{r,\gamma}\ \mathrm{d}p_\gamma^r, \tag{C.15f}
$$

$$
G_N^m = \sum_{\beta\in\mathbb{A}} \int_{\hat{\Gamma}_\mathrm{N}} \phi^m(\boldsymbol{y}) \boldsymbol{e}_\beta^m(\boldsymbol{y}) \cdot \boldsymbol{Y}_N\ \mathrm{d}\hat{\Gamma} \int_{I_\mathrm{p}^\beta} p_\beta^m P_N^{m,\beta} \mathrm{d}p_\beta^m \prod_{q\neq m} \int_{I_\mathrm{b}} B_N^q \mathrm{d}b^q \prod_{\substack{q\neq m\\ \gamma\neq\beta}} \int_{I_\mathrm{p}^\gamma} P_N^{q,\gamma}\ \mathrm{d}p_\gamma^q, \tag{C.15g}
$$

$$
f_{0,N}^{m,\beta} = \sum_{q\neq m} \sum_{\gamma\neq\beta} \int_{\hat{\Gamma}_\mathrm{N}} \phi^q(\boldsymbol{y}) \boldsymbol{e}_\gamma^q(\boldsymbol{y}) \cdot \boldsymbol{Y}_N\ \mathrm{d}\hat{\Gamma} \int_{I_\mathrm{b}} \int_{I_\mathrm{x}} \rho(x,b^q)\ X_N\ B_N^q\ \mathrm{d}x\ \mathrm{d}b^q \int_{I_\mathrm{p}^\gamma} p_\gamma^q\ P_N^{q,\gamma}\ \mathrm{d}p_\beta^m \times \prod_{r\neq q} \int_{I_\mathrm{b}} B_N^r\ \mathrm{d}b^r \prod_{\substack{r\neq\{m,q\}\\ \eta\neq\{\beta,\gamma\}}} \int_{I_\mathrm{p}^\eta} P_N^{r,\eta}\ \mathrm{d}p_\eta^r, \tag{C.15h}
$$

$$
f_{1,N}^{m,\beta} = \int_{\hat{\Gamma}_\mathrm{N}} \phi^m(\boldsymbol{y}) \boldsymbol{e}_\beta^m(\boldsymbol{y}) \cdot \boldsymbol{Y}_N\ \mathrm{d}\hat{\Gamma} \int_{I_\mathrm{b}} \int_{I_\mathrm{x}} \rho(x,b^m)\ X_N\ B_N^m\ \mathrm{d}x\ \mathrm{d}b^m \prod_{q\neq m} \int_{I_\mathrm{b}} B_N^q\ \mathrm{d}b^q \prod_{\substack{q\neq m\\ \gamma\neq\beta}} \int_{I_\mathrm{p}^\gamma} P_N^{q,\gamma}\ \mathrm{d}p_\gamma^q. \tag{C.15i}
$$

References

[1] R. Skrypnyk, J.C.O. Nielsen, M. Ekh, B.A. Pålsson, Metamodelling of wheel–rail normal contact in railway crossings with elasto-plastic material behaviour, Eng. Comput. 35 (1) (2019) 139–155, http://dx.doi.org/10.1007/s00366-018-0589-3, [Online]. Available: http://link.springer.com/10.1007/s00366-018-0589-3.

[2] R. Skrypnyk, M. Ekh, J.C.O. Nielsen, B.A. Pålsson, Prediction of plastic deformation and wear in railway crossings – Comparing the performance of two rail steel grades, Wear 428–429 (2019) 302–314, http://dx.doi.org/10.1016/j.wear.2019.03.019, [Online]. Available: https://www.sciencedirect.com/science/article/pii/S0043164818308081.

[3] R. Skrypnyk, B.A. Pålsson, J.C.O. Nielsen, M. Ekh, On the influence of crossing angle on long-term rail damage evolution in railway crossings, Int. J. Rail Transp. 9 (6) (2021) 503–519, http://dx.doi.org/10.1080/23248378.2020.1864794.

[4] R. Skrypnyk, U. Ossberger, B.A. Pålsson, M. Ekh, J.C.O. Nielsen, Long-term rail profile damage in a railway crossing: Field measurements and numerical simulations, Wear 472–473 (2021) http://dx.doi.org/10.1016/j.wear.2020.203331, [Online]. Available: https://www.sciencedirect.com/science/article/pii/S004316482030079X.

[5] C. Ansin, B.A. Pålsson, M. Ekh, F. Larsson, R. Larsson, Simulation and field measurement of the long-term rail surface damage due to plasticity, wear and surface rolling contact fatigue cracks in a curve, in: 12th International Conference on Contact Mechanics and Wear of Rail/Wheel Systems, Melbourne, Australia, 2022, p. 11.

[6] J.L. Lumley, The structure of inhomogeneous turbulent flows, in: Atmospheric Turbulence and Radio Wave Propagation, 1967, pp. 166–178, Publisher: Nauka, [Online]. Available: https://cir.nii.ac.jp/crid/1574231874542771712.

[7] G. Berkooz, P. Holmes, J.L. Lumley, The proper orthogonal decomposition in the analysis of turbulent flows, Annu. Rev. Fluid Mech. 25 (1) (1993) 539–575, http://dx.doi.org/10.1146/annurev.fl.25.010193.002543.

[8] A. Quarteroni, A. Manzoni, F. Negri, Reduced Basis Methods for Partial Differential Equations: an Introduction, Springer, 2015.

[9] F. Chinesta, R. Keunings, A. Leygue, The Proper Generalized Decomposition for Advanced Numerical Simulations, in: SpringerBriefs in Applied Sciences and Technology, Springer International Publishing, Cham, 2014, http://dx.doi.org/10.1007/978-3-319-02865-1, [Online]. Available: http://link.springer.com/10.1007/978-3-319-02865-1.

[10] P. Ladavèze, New algorithms: mechanical framework and development, C. R. Acad. Sci. 300 (2) (1985) 41–44.

[11] P. Ladevèze, A. Nouy, On a multiscale computational strategy with time and space homogenization for structural mechanics, Multiscale Computational Mechanics for Materials and Structures, Comput. Methods Appl. Mech. Engrg. 192 (28) (2003) 3061–3087, http://dx.doi.org/10.1016/S0045-7825(03)00341-4, [Online]. Available: https://www.sciencedirect.com/science/article/pii/S0045782503003414.

[12] P. Ladevèze, J.C. Passieux, D. Néron, The LATIN multiscale computational method and the Proper Generalized Decomposition, Multiscale Models and Mathematical Aspects in Solid and Fluid Mechanics, Comput. Methods Appl. Mech. Engrg. 199 (21) (2010) 1287–1296, http://dx.doi.org/10.1016/j.cma.2009.06.023, [Online]. Available: https://www.sciencedirect.com/science/article/pii/S0045782509002643.

[13] P. Ladeveze, Nonlinear Computational Structural Mechanics: New Approaches and Non-Incremental Methods of Calculation, Springer Science & Business Media, 2012.

[14] A. Ammar, B. Mokdad, F. Chinesta, R. Keunings, A new family of solvers for some classes of multidimensional partial differential equations encountered in kinetic theory modeling of complex fluids, J. Non-Newton. Fluid Mech. 139 (3) (2006) 153–176, http://dx.doi.org/10.1016/j.jnnfm.2006.07.007, [Online]. Available: https://www.sciencedirect.com/science/article/pii/S0377025706001662.

[15] A. Ammar, B. Mokdad, F. Chinesta, R. Keunings, A new family of solvers for some classes of multidimensional partial differential equations encountered in kinetic theory modelling of complex fluids: Part II: Transient simulation using space-time separated representations, J. Non-Newton. Fluid Mech. 144 (2) (2007) 98–121, http://dx.doi.org/10.1016/j.jnnfm.2007.03.009, [Online]. Available: https://www.sciencedirect.com/science/article/pii/S0377025707000821.

[16] A. Ammar, F. Chinesta, P. Diez, A. Huerta, An error estimator for separated representations of highly multidimensional models, Comput. Methods Appl. Mech. Engrg. 199 (25) (2010) 1872–1880, http://dx.doi.org/10.1016/j.cma.2010.02.012, [Online]. Available: https://www.sciencedirect.com/science/article/pii/S0045782510000708.

[17] F. Chinesta, A. Ammar, E. Cueto, Recent advances and new challenges in the use of the Proper Generalized Decomposition for solving multidimensional models, Arch. Comput. Methods Eng. 17 (4) (2010) 327–350, http://dx.doi.org/10.1007/s11831-010-9049-y.

[18] A. Ammar, M. Normandin, F. Chinesta, Solving parametric complex fluids models in rheometric flows, J. Non-Newton. Fluid Mech. 165 (23) (2010) 1588–1601, http://dx.doi.org/10.1016/j.jnnfm.2010.08.006, [Online]. Available: https://www.sciencedirect.com/science/article/pii/S037702571000217X.

[19] E. Pruliere, F. Chinesta, A. Ammar, On the deterministic solution of multidimensional parametric models using the Proper Generalized Decomposition, Math. Comput. Simulation 81 (4) (2010) 791–810, http://dx.doi.org/10.1016/j.matcom.2010.07.015, [Online]. Available: https://www.sciencedirect.com/science/article/pii/S0378475410002521.

[20] X. Zou, M. Conti, P. Díez, F. Auricchio, A nonintrusive proper generalized decomposition scheme with application in biomechanics, Internat. J. Numer. Methods Engrg. 113 (2) (2018) 230–251, http://dx.doi.org/10.1002/nme.5610, [Online]. Available: https://onlinelibrary.wiley.com/doi/abs/10.1002/nme.5610.

[21] E. Giner, B. Bognet, J.J. Ródenas, A. Leygue, F.J. Fuenmayor, F. Chinesta, The Proper Generalized Decomposition (PGD) as a numerical procedure to solve 3D cracked plates in linear elastic fracture mechanics, Int. J. Solids Struct. 50 (10) (2013) 1710–1720, http://dx.doi.org/10.1016/j.ijsolstr.2013.01.039, [Online]. Available: https://www.sciencedirect.com/science/article/pii/S0020768313000541.

[22] D. González, A. Ammar, F. Chinesta, E. Cueto, Recent advances on the use of separated representations, Internat. J. Numer. Methods Engrg. 81 (5) (2010) 637–659, http://dx.doi.org/10.1002/nme.2710, [Online]. Available: https://onlinelibrary.wiley.com/doi/abs/10.1002/nme.2710.

[23] E. Cueto, D. González, I. Alfaro, Proper Generalized Decompositions, in: SpringerBriefs in Applied Sciences and Technology, Springer International Publishing, Cham, 2016, http://dx.doi.org/10.1007/978-3-319-29994-5, [Online]. Available: http://link.springer.com/10.1007/978-3-319-29994-5.

[24] B. Bognet, F. Bordeu, F. Chinesta, A. Leygue, A. Poitou, Advanced simulation of models defined in plate geometries: 3D solutions with 2D computational complexity, Comput. Methods Appl. Mech. Engrg. 201–204 (2012) 1–12, http://dx.doi.org/10.1016/j.cma.2011.08.025, [Online]. Available: https://www.sciencedirect.com/science/article/pii/S0045782511002891.

[25] B. Bognet, A. Leygue, F. Chinesta, On the fully 3D simulations of thermoelastic models defined in plate and shell geometries, Eur. J. Comput. Mech. 21 (1–2) (2012) 40–51, http://dx.doi.org/10.1080/17797179.2012.702429, [Online]. Available: https://www.tandfonline.com/doi/full/10.1080/17797179.2012.702429.

[26] H. Hertz, On the contact of solid, elastic bodies, J. Reine Angew. Math. 92 (1882) 156–171.

[27] J.J. Kalker, Three-Dimensional Elastic Bodies in Rolling Contact, Springer Science & Business Media, 1990.

[28] J.J. Kalker, Wheel-rail rolling contact theory, Wear 144 (1) (1991) 243–261, http://dx.doi.org/10.1016/0043-1648(91)90018-P, [Online]. Available: https://www.sciencedirect.com/science/article/pii/004316489190018P.

[29] J. Ayasse, H. Chollet, Determination of the wheel rail contact patch in semi-Hertzian conditions, Veh. Syst. Dyn. 43 (3) (2005) 161–172, http://dx.doi.org/10.1080/00423110412331327193.

[30] X. Quost, M. Sebes, A. Eddhahak, J.-B. Ayasse, H. Chollet, P.-E. Gautier, F. Thouverez, Assessment of a semi-Hertzian method for determination of wheel–rail contact patch, Veh. Syst. Dyn. 44 (10) (2006) 789–814, http://dx.doi.org/10.1080/00423110600677948.